

NASA Contractor Report CR-2003-211187

A New Objective Technique for Verifying Mesoscale Numerical Weather Prediction Models

Prepared By:

The Applied Meteorology Unit

Prepared for:

Kennedy Space Center
Under Contract NAS10-01052

NASA
National Aeronautics and
Space Administration

Office of Management

Scientific and Technical
Information Program

2003

Attributes and Acknowledgments

NASA/KSC POC:

Dr. Francis J. Merceret

YA-D

Applied Meteorology Unit (AMU) / ENSCO Inc.

Jonathan L. Case

John Manobianco

Dynacs Inc.

John E. Lane

Christopher D. Immer

Executive Summary

An ongoing challenge in mesoscale numerical weather prediction (NWP) is to determine the best method for verifying the performance of high-resolution, detailed forecasts. Traditional objective techniques that evaluate NWP model performance based on point error statistics and precipitation threat scores can no longer accurately represent the skill of mesoscale NWP models as resolutions continue to increase along with available computing power. Subjective evaluation techniques are very costly and time-consuming. As a result, objective phenomenological-based verification methodologies are required in order to determine the representative skill and added value of high-resolution NWP models.

This report presents a new objective technique to verify predictions of the sea-breeze phenomenon over east-central Florida by the Regional Atmospheric Modeling System (RAMS) mesoscale numerical weather prediction (NWP) model. The Contour Error Map (CEM) technique identifies sea-breeze transition times in objectively-analyzed grids of observed and forecast wind, verifies the forecast sea-breeze transition times against the observed times, and computes the mean post-sea breeze wind direction and speed to compare the observed and forecast winds behind the sea-breeze front.

The CEM technique is superior to traditional objective verification techniques and previously-used subjective verification methodologies because:

- It is automated, requiring little manual intervention,
- It accounts for both spatial and temporal scales and variations,
- It accurately identifies and verifies the sea-breeze transition times, and
- It provides verification contour maps and simple statistical parameters for easy interpretation.

The CEM uses a parallel lowpass boxcar filter and a high-order bandpass filter to identify the sea-breeze transition times in the observed and model grid points. Once the transition times are identified, CEM fits a Gaussian histogram function to the actual histogram of transition time differences between the model and observations. The fitted parameters of the Gaussian function subsequently explain the timing bias and variance of the timing differences across the valid comparison domain. Once the transition times are all identified at each grid point, the CEM computes the mean wind direction and speed during the remainder of the day for all times and grid points after the sea-breeze transition time.

The CEM technique performed quite well when compared to independent meteorological assessments of the sea-breeze transition times and results from a previously published subjective evaluation. The algorithm correctly identified a forecast or observed sea-breeze occurrence or absence 93% of the time during the two-month evaluation period from July and August 2000. Nearly all failures in CEM were the result of complex precipitation features (observed or forecast) that contaminated the wind field, resulting in a false identification of a sea-breeze transition. A qualitative comparison between the CEM timing errors and the subjectively determined observed and forecast transition times indicate that the algorithm performed very well overall. Most discrepancies between the CEM results and the subjective analysis were again caused by observed or forecast areas of precipitation that led to complex wind patterns. The CEM also failed on a day when the observed sea-breeze transition affected only a very small portion of the verification domain.

Based on the results of CEM, the RAMS tended to predict the onset and movement of the sea-breeze transition too early and/or quickly. The domain-wide timing biases provided by CEM indicated an early bias on 30 out of 37 days when both an observed and forecast sea breeze occurred over the same portions of the analysis domain. These results are consistent with previous subjective verifications of the RAMS sea breeze predictions. A comparison of the mean post-sea breeze winds indicate that RAMS has a positive wind-speed bias for all days, which is also consistent with the early bias in the sea-breeze transition time since the higher wind speeds resulted in a faster inland penetration of the sea breeze compared to reality.

Table of Contents

Executive Summary.....	iii
Table of Contents	iv
List of Figures	v
List of Tables.....	vi
1. Introduction	1
2. Model and Observational Data	2
2.1 RAMS Configuration.....	2
2.2 Data Preparation.....	3
3. Sea-Breeze Detection and Verification Methodology.....	5
3.1 Contour Error Map Algorithm Development.....	5
3.2 Sea-Breeze Transition Time Estimation Filter	7
3.3 Sample Output from 18 July 2000	11
3.4 Image Erosion to Suppress Contamination by River Breezes.....	14
4. Algorithm Validation and Results	17
4.1 Validation of CEM.....	17
4.2 Interpreting Objective Model Verification Results	20
4.3 Mean Post-Sea Breeze Wind Comparisons.....	21
5. Summary.....	22
6. References	23
Appendix A: Gradient Search Method to Fit Gaussian Probability Function	24
Appendix B: Band Pass Filter Details	26
List of Abbreviations and Acronyms	33

List of Figures

Figure 1.	The RAMS domains for the 60-km mesh grid (grid 1) covering much of the southeastern United States and adjacent coastal waters, the 15-km mesh grid (grid 2) covering the Florida peninsula and adjacent coastal waters, the 5-km mesh grid (grid 3) covering east-central Florida and adjacent coastal waters, and the 1.25-km mesh grid (grid 4) covering the area immediately surrounding KSC/CCAFS.	3
Figure 2.	The locations of the 44 KSC/CCAFS observational towers used to verify the RAMS forecast sea breezes over east-central Florida.	4
Figure 3.	The CEM algorithm block diagram illustrating the order of processing to generate verification data fields.	7
Figure 4.	The sea breeze filter signal processing block diagram.	7
Figure 5.	Results of SB filter from Figure 4, applied to wind direction data from 24–31 July 2000.	8
Figure 6.	Results of SB filter from Figure 4, applied to wind direction data from 24–31 July 2000.	11
Figure 7.	Hourly sequence of objectively analyzed tower winds at 54 ft, valid on 18 July 2000 at (a) 1600 UTC, (b) 1700 UTC, (c) 1800 UTC, and (d) 1900 UTC.	12
Figure 8.	Hourly sequence of objectively analyzed RAMS forecast winds (interpolated to 54 ft) from the 1.25-km grid, initialized at 1200 UTC 18 July.	13
Figure 9.	Sample output of the CEM algorithm for 18 July 2000.	14
Figure 10.	Sea-breeze transition times for 12 July 2000.	15
Figure 11.	Erosion based on the gradient of the SB transition time of the observed wind field on 18 August 2000: (a) Before erosion, and (b) after erosion.	16
Figure 12.	Mean post-SB winds based on eroded SB transition times: (a) Mean wind speeds for July 2000, (b) Mean wind speed for August 2000, (c) Mean wind direction for July 2000, and (d) Mean wind direction for August 2000.	21
Figure A1.	Sample CEM histogram showing Gaussian fit from equation (A1).	24
Figure B1.	Cascaded Nth order IIR bandpass filter network.	26
Figure B2.	Single second order section of cascaded bandpass filter network.	26
Figure B3.	Gain response of 8th Order (M=4) Butterworth bandpass filter, showing equivalent gain response of each individual second order section for $f_0=300$ Hz and $Q=0.33$ (top), and $Q=1.0$ (bottom).	27
Figure B4.	Gain (top panel) and phase response (bottom panel) of digital 4th order (M=2) bandpass Butterworth filter with $f_s = 11025$ Hz and $Q = 0.25$	29
Figure B5.	Gain (top panel) and phase response (bottom panel) of digital 12th order (M=6) bandpass Butterworth filter with $f_s = 11025$ Hz and $Q = 1$	30
Figure B6.	Gain response of 2nd, 4th, 8th, and 16th order Butterworth bandpass filters with $Q = 0.33$, $f_0 = 300$, and $f_s = 11025$ Hz.	32

List of Tables

Table 1.	A summary of the grid configuration parameters for all four RAMS grids.	3
Table 2.	Filter output showing the SB code* and SB transition time (if any) for observed data from July 2000 at grid coordinate $x = 55, y = 42$	9
Table 3.	Filter output showing the SB code* and SB transition time (if any) for observed data from July 2000 at grid coordinate $x = 51, y = 35$	10
Table 4.	Gaussian fit parameters for eroded CEM histograms and subjectively-determined range of observed and RAMS times of the SB transition (in UTC) for July 2000.	18
Table 5.	Gaussian fit parameters for eroded CEM histograms, and subjectively-determined range of observed and RAMS times of the SB transition (in UTC) for August 2000.	19

1. Introduction

Mesoscale weather prediction involves forecasts for specific locations at precise times, such as a wind forecast for launch complex 39A at 0700. Numerical Weather Prediction (NWP) models are in widespread operational use for general regional and global forecasts, but the technology still needs improvement for application and performance evaluation at the mesoscale. An ongoing difficulty in mesoscale NWP is to determine the best method for verifying the performance of high-resolution, detailed forecasts. Traditional objective techniques that evaluate NWP model performance based on point error statistics and precipitation threat scores can no longer accurately represent the skill of mesoscale NWP models as resolutions continue to increase along with available computing power. Subjective evaluation techniques are very costly and time-consuming. As a result, objective phenomenological-based verification methodologies are required in order to determine the representative skill and added value of high-resolution NWP models.

A coordinated effort between personnel from Dynacs, Inc. and the Applied Meteorology Unit (operated by ENSCO Inc.) was established in order to develop advanced technologies for objectively evaluating the performance of the Regional Atmospheric Modeling System (RAMS; Pielke et al. 1992) mesoscale NWP model, currently used operationally on the Eastern Range. These technologies were applied to evaluate model performance in forecasting the sea breeze (SB) phenomenon over east-central Florida. The verification of the SB was chosen because this phenomenon occurs quite frequently in east-central Florida, particularly in the spring and summer months. In addition, the SB can significantly impact space operations due to the sharp wind shifts and thunderstorm development often associated with SB transition zones.

Some recent studies have addressed the deficiencies in applying traditional objective verification statistics to mesoscale models, and presented alternative means for verifying phenomena in mesoscale models. Nutter and Manobianco (1999) and Manobianco and Nutter (1999) performed an objective point verification and subjective phenomenological verification, respectively, of the 29-km version of the National Center for Environmental Prediction (NCEP) meso-Eta model. Case et al. (2002) performed both an objective and subjective verification of RAMS during the 2000 Florida summer, including a validation of the model predicted SB and daily thunderstorm initiation. These studies demonstrated that objective point error statistics alone (i.e. measures-oriented approach) cannot adequately determine a mesoscale model's utility, and that phenomenological verification is also required as part of the validation process. While these studies successfully quantified the value of the mesoscale models in predicting specific meteorological phenomena, a manual subjective intervention was used to perform the phenomenological verification, which can be quite expensive in terms of the required manpower resources.

Recent efforts presented by Baldwin et al. (2001) and Baldwin et al. (2002) have demonstrated the need for an improved, events-oriented technique for precipitation verification rather than the traditional measures-oriented or distributions-oriented methods of verification. Baldwin et al. (2001) illustrated the problem by showing a theoretical distribution of observed precipitation with embedded heavy cells. The authors then verified two hypothetical forecast fields, one with a smooth precipitation pattern without any embedded cells and another with a very similar pattern to the simulated observed field, but slightly out of phase. The authors demonstrated the failure of traditional measures-oriented and distributions-oriented approaches in that the smooth forecast field generated better statistics (i.e. root mean square error, bias, threat score, and correlation coefficient) despite appearing less realistic than the other forecast precipitation pattern. Baldwin et al. (2002) built upon this premise by developing an events-oriented verification technique using a cluster analysis on different modes of precipitation patterns.

The primary goal of this project has been to develop algorithms and software to demonstrate a proof-of-concept procedure to automatically detect and identify a SB from forecast and observational wind data, and compare the two SB data sets in a meaningful, quantitative manner for verification. The initial strategy was based on processing a time sequence of images in the spatial domain, since it seemed logical that the observed features of interest are mostly visible in the spatial domain. This initial strategy was not entirely successful since the SB feature is not always apparent in single spatial images. Therefore, a robust methodology was developed to treat the spatial and temporal data simultaneously.

The remainder of this report is organized as follows. Section 2 describes the observed data and RAMS model configuration used to develop the objective technique for verifying the SB phenomenon. Section 3 explains the methodology used to develop the objective SB verification technique and provides some example output. Section 4 presents a validation of the objective algorithm and the verification results and Section 5 summarizes the report.

2. Model and Observational Data

2.1 RAMS Configuration

The three-dimensional, non-hydrostatic mode of RAMS (version 4a) was run on four nested grids with a horizontal grid spacing of 60, 15, 5, and 1.25 km (Figure 1). RAMS uses a stretched vertical coordinate from near the surface up to 18195 m, with additional vertical levels in grids 3 and 4 to provide enhanced vertical resolution near the ground. A summary of the horizontal and vertical grid parameters is provided in Table 1. The physical parameterization schemes used in ERDAS RAMS include a microphysics scheme following Cotton et al. (1982), a modified Kuo cumulus convection scheme (Tremback 1990), the Chen and Cotton (1988) radiation scheme, a Mellor and Yamada (1982) type turbulence closure, and an 11-layer soil-vegetation model (Tremback and Kessler 1985) with fixed soil moisture in the initial condition. The modified Kuo scheme is run on grids 1–3 whereas grid 4 utilizes explicit convection only. The mixed-phase microphysics scheme is run on all four grids.

RAMS is initialized twice-daily at 0000 and 1200 UTC using the Eta 12-h forecast grids from its forecast cycle 12 hours earlier (due to operational time constraints), as well as available observational data including the CCAFS rawinsonde (XMR), Aviation Routine Weather Reports (METAR), buoys, and KSC/CCAFS wind-tower, 915-MHz, and 50-MHz Doppler Radar Wind Profiler data. No variational data assimilation or nudging technique is applied when incorporating observational data. Instead, RAMS is initialized from a cold start by integrating the model forward in time from a gridded field without any balancing or data assimilation steps. Observational data are analyzed onto hybrid coordinates using the RAMS Isentropic Analysis (ISAN) package (Tremback 1990). The ISAN hybrid coordinate consists of a combination of isentropes and terrain-following surfaces on which data are analyzed within the RAMS model domain, similar to the NCEP Rapid Update Cycle model (Benjamin et al. 1998). For sea-surface temperature initialization, RAMS uses fixed monthly climatological means on grid 1, and these values are subsequently interpolated to the inner grids. The lateral boundary conditions are nudged (Davies 1983) by 12–36-h forecasts from the NCEP Eta model, interpolated onto an 80-km grid. Output from the Eta model is available every 6 h for boundary conditions to RAMS. Two-way interactive boundary conditions are used on the inner three nested grids.

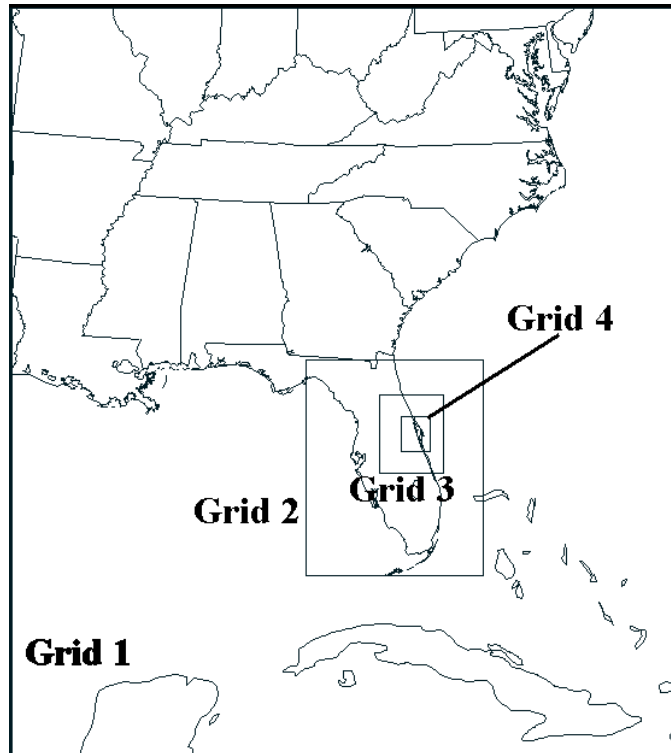


Figure 1. The RAMS domains for the 60-km mesh grid (grid 1) covering much of the southeastern United States and adjacent coastal waters, the 15-km mesh grid (grid 2) covering the Florida peninsula and adjacent coastal waters, the 5-km mesh grid (grid 3) covering east-central Florida and adjacent coastal waters, and the 1.25-km mesh grid (grid 4) covering the area immediately surrounding KSC/CCAFS.

Table 1. A summary of the grid configuration parameters for all four RAMS grids. The model parameters include the number of grid points in the x, y, and z directions (n_x , n_y , and n_z), horizontal grid spacing (dx), minimum and maximum vertical resolutions (dz_{min} and dz_{max}), and the heights of the minimum and maximum physical vertical levels (z_{-min} and z_{-max}), with all distances given in meters.

Grid	n_x	n_y	n_z	dx (m)	dz_{min} (m)	dz_{max} (m)	z_{-min}^* (m)	z_{-max} (m)
1	36	40	33	60000	50	750	23	18195
2	38	46	33	15000	50	750	23	18195
3	41	50	36	5000	25	750	11	18195
4	74	90	36	1250	25	750	11	18195

* z_{-min} actually represents the 2nd vertical level, which is the first model level above ground. For computational purposes, the height of the first model level for each grid is below ground at -20, -20, -11, and -11 m for grids 1, 2, 3, and 4, respectively.

2.2 Data Preparation

This study used the high-resolution network of 44 wind towers across KSC/CCAFS (Figure 2) in conjunction with NWP forecasts from RAMS for July and August 2000. The KSC/CCAFS tower network has an average station spacing of ~ 5 km and the data archive provided wind information every five minutes. The RAMS NWP model output from the innermost grid 4 centered on KSC/CCAFS was used for the development of the SB verification algorithm.

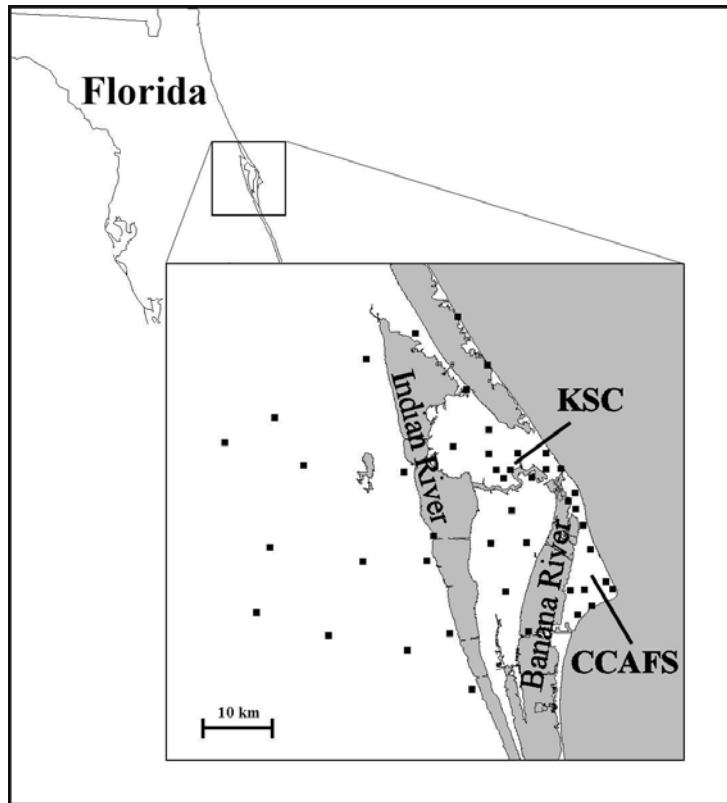


Figure 2. The locations of the 44 KSC/CCAFS observational towers used to verify the RAMS forecast sea breezes over east-central Florida.

The original operational RAMS forecast output was saved only once per hour due to disk space limitations on the operational system. This relatively coarse time resolution presented a limiting factor for the robustness of an objective verification technique. As a result, the daily RAMS forecasts were re-run for all of July and August 2000 in order to generate NWP model output every five minutes, consistent with the time resolution of the observed tower data.

To conduct a head-to-head comparison between the observed and forecast fields, the gridded RAMS forecasts were interpolated to the location and height of the KSC/CCAFS tower observations. Then, the observed and point forecast winds were analyzed objectively onto the 1.25-km RAMS forecast grid using identical parameters of the Barnes (1964) algorithm. As a result, the objective analysis grid of observations and forecasts has coverage only within the domain of the KSC/CCAFS wind-tower network shown in Figure 2.

The motivation for re-analyzing point forecast data on the 1.25-km RAMS forecast grid was threefold:

- The original RAMS gridded forecasts contains wind information over both land and water, whereas the KSC/CCAFS tower observations are located solely over land. By interpolating RAMS forecasts from the original grid to the tower locations and then analyzing the observed and point forecast data back to the RAMS grid, the resulting objective analysis will represent a fair comparison between the observed and forecast wind fields.
- Re-analyzing point forecast data at each tower location results in observed and forecast wind fields with similar resolvable scales of motion.
- Objectively analyzing data onto a grid with evenly-spaced points provides a favorable platform for both analysis and display purposes.

3. Sea-Breeze Detection and Verification Methodology

3.1 Contour Error Map Algorithm Development

The predominant mesoscale feature across the Florida peninsula during the summer months is the land-sea breeze oscillation (LSBO). Intense solar heating during the day creates a thermal contrast between air over land (T_a) and air over the water (T_w). When T_a exceeds T_w sufficiently, a thermally-induced direct circulation results in the lowest few kilometers of the atmosphere. Near the surface, air flows from the cooler air mass residing over water to the warmer air mass over land, whereas a return circulation aloft flows from land to water. A boundary interface or SB “front” often develops at the leading edge of the SB circulation, and advances inland as the day progresses. Air rises along this leading edge while air descends above the water, completing the direct circulation.

At night, the SB circulation collapses after the thermal contrast between land and water weakens, resulting in surface winds blowing from land to water (i.e. the land breeze). The land-breeze circulation is generally weaker than the sea breeze in both velocity and height of development since the ocean-based heat source for the land breeze is much weaker than the land-based heat source for the SB circulation (Atkinson 1981).

Attempting to observe a SB passage from a sequence of spatial images is a logical first approach to this problem. Whether using a subjective manual method incorporating an animated image loop or an objective automatic method of detection, the spatial gradient of wind direction (and/or wind speed) is the observed feature of interest, representing the SB transition zone.

To determine the occurrence and timing of the sea-breeze passage, the development and maintenance of a wind-shift from an offshore to an onshore wind component must occur. During prevailing easterly (onshore) flow, an increase in wind speed can occur during the morning hours, signifying a sea-breeze passage; however, these sea breezes tend to be weak and are not taken into account for this study. These wind direction criteria were applied to both the observed and RAMS forecasts to determine the forecast sea-breeze passage. The coastline of east-central Florida is approximately oriented along a 335-155° line; however, for the purposes of simplifying the initial technique development, wind directions between 0° and 180° were considered onshore winds, while 180° to 360° wind directions were defined as offshore.

A sea-breeze front along Florida’s east coast is often accompanied by a sharp clearing line and reflectivity fine-line that propagate westward with time. Radar images of radar reflectivity often show a distinct SB transition zone within spatial extents on the order of 100 km or more. Problems can arise when observing reflectivity or wind data over smaller spatial extents, such as that associated with the KSC/CCAFS wind tower network. In addition, local conditions over the KSC/CCAFS region include effects from the Indian and Banana rivers (river breezes, see Fig. 2), as well as convective thunderstorm activity, which often corrupt and mask the SB passage over this small mesoscale region. In addition, the wind direction field occasionally changes gradually, which results in a small spatial gradient rather than a distinct frontal transition from offshore to onshore flow.

Two objective techniques were examined to identify and compare forecast versus observed SB boundaries using gridded observed and RAMS forecast data. During the first portion of the project, a method was developed that utilized image-processing methods to identify gradients in wind direction and wind speed. The algorithm underwent extensive tuning, but the boundaries identified by the algorithm were typically discontinuous and noisy.

A second approach, named Contour Error Map (CEM) was then examined using a binary threshold to distinguish between easterly (onshore) and westerly (offshore) wind directions. This method incorporated both spatial and temporal wind data at each grid point to identify observed and forecast SB transition times. A filtering technique was implemented to identify the correct transition times from offshore to onshore wind flow. To ensure focus on the SB boundary only, an erosion technique was introduced to remove extraneous boundaries not associated with the primary SB front, such as river breezes and precipitation outflow boundaries. The components of the CEM method are described in more detail below.

The resultant version I of CEM gave the time bias (forecast – observed) of wind-direction transition from offshore to onshore. A histogram of SB transition times was also generated and a Gaussian histogram function

\hat{h}_k was fitted (see Appendix A) to the CEM histogram h_k in order to quantify and parameterize the comparison in terms of four quantities:

- $\tau \equiv$ mean bias
- $\sigma \equiv$ standard deviation of bias
- $f_O \equiv$ fractional grid area with only observed SB transition
- $f_R \equiv$ fractional grid area with only RAMS SB transition

The form of the Gaussian histogram function used in this study is given by:

$$\hat{h}_k = \frac{1 - f_O - f_R}{\sigma\sqrt{2\pi}} \Delta t e^{-(t_k - \tau)^2 / 2\sigma^2} \quad (1)$$

where t_k is the time corresponding to h_k , the subscript k corresponds to the k th 5-minute bin (the forecast – observed SB transition time difference), and $\Delta t = 5$ min (the time interval between successive observed and forecast wind fields).

For days with an overlapping observed and forecast SB transition within the grid domain, the Gaussian function fit was performed to produce a set of parameters that describe the quality of the RAMS forecast SB. Days that have small mean biases and standard deviations of the bias indicate more skillful forecasts of the SB transition timing and movement. In addition, the mean wind direction and wind speed was computed on the seaward side of the SB transitions in order to determine the skillfulness of RAMS in predicting the movement of the SB boundary, as well as the characteristics of the post-SB wind environment. The calculations were made for all times and grid points following a SB transition.

The CEM-I binary detection scheme appeared useful, but its performance suffered when the LSBO signal was contaminated by microscale convective winds, river breezes, or synoptic wind shifts. In some cases, the LSBO signal was small compared to the synoptic background. A synoptic shift, coupled with relatively small amplitude LSBO, resulted in the CEM-I binary wind direction analysis being inadequate to detect and quantify a SB passage for a wide range of cases.

As a result, a second version of CEM was developed to build upon the framework of CEM-I by adding a time estimation filter to determine the SB transition times in both the observed and forecast grids. Each grid point was processed individually by a detector composed of a parallel lowpass (LP) boxcar filter (Rabiner and Gold 1975) and a high-order bandpass (BP) filter (Hillman and Lane 1989) centered on a frequency of 1/day (refer to Appendix B for filter details). The LP filter was used to remove microscale, convective features with a frequency on the order of 1/minute, whereas the BP filter was designed to simulate the LSBO for a 24-h periodic cycle, as observed in nature. After each grid point was pre-processed by the SB filter, the spatial image was reconstructed.

The CEM-II algorithm (hereafter referred to as simply CEM) consists of four sections, as shown in Figure 3:

- (1) Point Processing: Calculates the sine of wind direction at each point in x , y , and t space.
- (2) Temporal Processing: Processes a continuous time series at each x - y grid point to determine a best estimate of the offshore to onshore wind transition time.
- (3) Spatial Processing: Computes two-dimensional spatial gradients of SB filtered and recombined spatial images.
- (4) Comparison and Analysis: Compares RAMS and observed fields for similarities using the Gaussian fitted function and corresponding parameters defined in the CEM-I section, as well as computing the mean post-SB wind direction and speed.

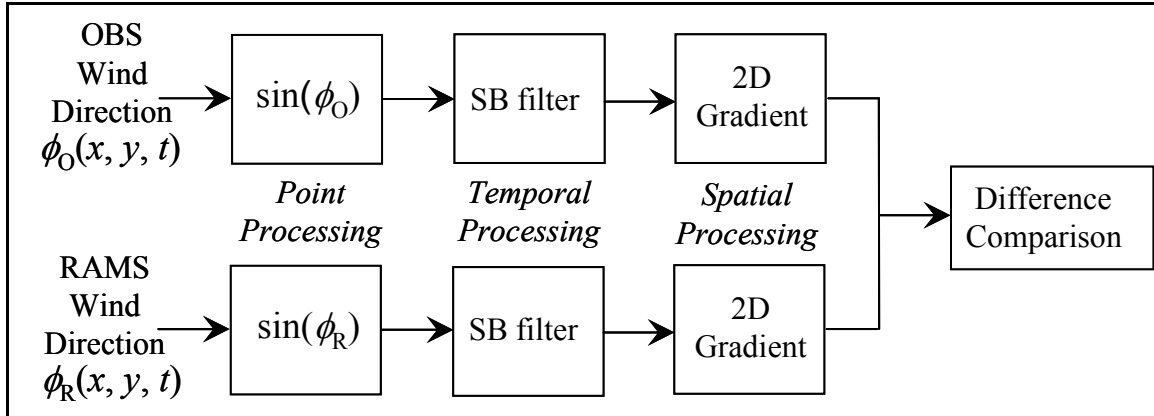


Figure 3. The CEM algorithm block diagram illustrating the order of processing to generate verification data fields.

3.2 Sea-Breeze Transition Time Estimation Filter

The SB time estimation filter can be considered as a SB transition time detector and estimator made up of two filter sections: a low pass (LP) filter in parallel with a dual-band pass (BP) filter. The BP filter is based on a recursive or infinite impulse response (IIR) filter, whereas the LP filter is a non-recursive or finite impulse response (FIR) filter. The LP filter is implemented as a moving average of length $L = 31$ points, centered about the middle of the sliding window. The LP filter can also be considered as a FIR filter of length L where all coefficients are equal to unity.

The BP filter is based on an 8th-order, maximally-flat, Butterworth, IIR filter design. This filter type is not zero or linear phase; however, summing the outputs of two identical IIR filter structures, where the input data in the second filter is read in reverse order, results in a zero-phase recursive structure. The center frequency f_0 is set to match the 24-hour LSBO period. The BP filter is implemented by summing the outputs of two 8th-order filters with identical characteristics, where one filter processes a block of data forward in time, and the other filter processes the data backward in time from the end of the block.

The SB filter structure is not designed to be a real-time process because of the need to implement zero-phase filters. If the current SB filter were implemented in a real-time meteorological system, the BP filter structure would be linear phase with a minimum time delay of about 36 hours, based on this dual 8th-order IIR filter. In other words, based on current wind direction data, the result of the SB filter is to estimate the SB transition time no more recently than the previous day.

The signal processing strategy behind the SB transition time filter is summarized by Figure 4. The BP filter provides a SB transition time predictor, which is compared to the LP filtered wind direction signal at every spatial grid point. If the time difference between the predicted BP-SB time and the LP-SB time exceeds 6 hours, no SB for that day is assumed.

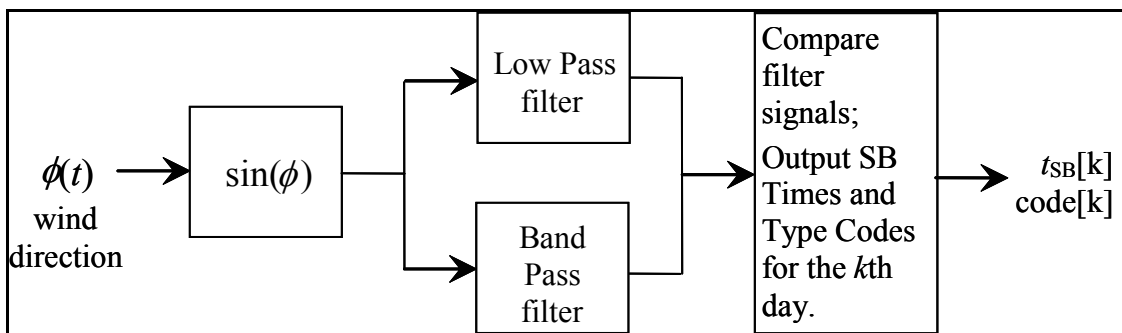


Figure 4. The sea breeze filter signal processing block diagram.

Every grid point in the observed and forecast data is processed using the SB filter technique of Figure 4. Recombining processed time domain data into spatial images results in two-dimensional grids of SB transition times. These grids of observed and forecast SB transition times were converted into the General Meteorological Package visualization and display software for analysis and presentation purposes.

Table 2 shows sample output using 5-min data for the month of July 2000 at grid location $x = 55, y = 42$. Note that the SB filter algorithm fills in missing data by performing a linear interpolation between end points around the missing data before the LP and BP sections. Figure 5 displays the corresponding filter outputs for the last eight days of the month, corresponding to the entries in Table 2. The raw data plotted in Figure 5 is the sine of the wind direction ϕ . In general, $\sin\phi$ would be replaced by $\sin(\phi - \phi_0)$, where ϕ_0 is the offset from true north (0°) as a result of the local orientation of the coastline (i.e. $335-155^\circ$). In this report, $\phi_0 = 0$.

Table 3 shows for comparison a grid point with a separation in the x direction of 5 km (westward) and a separation in the y direction of 8.75 km (southward) from the grid point data used in Table 2. Figure 6 displays the corresponding filter outputs for the last eight days of the month, corresponding to the entries in Table 3. As can be seen, there is a strong correlation in the time domain signals by comparing Figures 5 and 6.

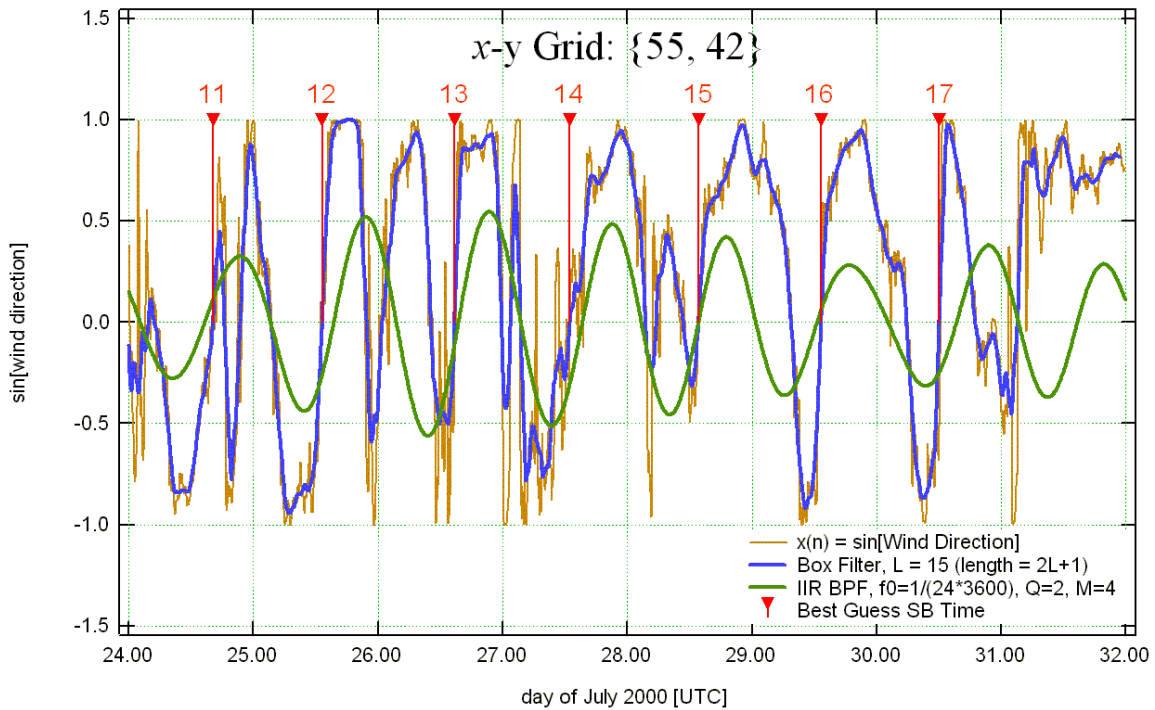


Figure 5. Results of SB filter from Figure 4, applied to wind direction data from 24–31 July 2000. Red sticks indicate the estimated SB transition times derived from the IIR BP filter (BPF) and LP filter.

Table 2. Filter output showing the SB code* and SB transition time (if any) for observed data from July 2000 at grid coordinate $x = 55$, $y = 42$. The SB transition times are given in units of UTC days of the month and local daylight time (LDT). Note that SB transition times are determined based on a changeover from offshore ($> 180^\circ$ wind direction) to onshore ($< 180^\circ$ wind direction).

Day	SB Code	Transition Time (UTC days)	Transition Time (LDT)
1	1	1.632	1110
2	1	2.477	0725
3	-2		
4	-2		
5	-4		
6	1	6.749	1355
7	-2		
8	1	8.675	1210
9	-2		
10	-2		
11	1	11.614	1045
12	1	12.705	1255
13	-2		
14	-4		
15	-2		
16	-2		
17	-2		
18	-4		
19	1	19.549	0910
20	-2		
21	1	21.730	1330
22	1	22.730	1330
23	1	23.682	1220
24	1	24.678	1215
25	1	25.552	0915
26	1	26.616	1050
27	1	27.540	0900
28	1	28.574	0945
29	1	29.558	0925
30	1	30.503	0805
31	-4		

*SB Code: 1 = SB transition occurrence.
-1 = Land breeze transition occurrence (not implemented).
-2 = No SB transition detected in low pass (LP) filtered signal.
-3 = Multiple SB transitions detected in band pass (BP) filtered signal.
-4 = SB time difference in LP and BP exceeds 6 hours.

Table 3. Filter output showing the SB code* and SB transition time (if any) for observed data from July 2000 at grid coordinate $x = 51$, $y = 35$. The SB transition times are given in units of UTC days of the month and local daylight time (LDT). Note that SB transition times are determined based on a changeover from offshore ($> 180^\circ$ wind direction) to onshore ($< 180^\circ$ wind direction).

Day	SB Code	Transition Time (UTC days)	Transition Time (LDT)
1	1	1.647	1130
2	1	2.462	0705
3	-2		
4	-2		
5	1	5.591	1010
6	1	6.743	1350
7	-2		
8	1	8.672	1205
9	-2		
10	-2		
11	1	11.629	1105
12	1	12.728	1330
13	1	13.831	1555
14	-4		
15	-2		
16	-2		
17	-2		
18	-4		
19	1	19.567	0935
20	-4		
21	1	21.798	1510
22	1	22.761	1415
23	1	23.712	1305
24	1	24.696	1240
25	1	25.561	0925
26	1	26.631	1110
27	1	27.561	0925
28	1	28.571	0940
29	1	29.564	0930
30	1	30.500	0800
31	-4		

*SB Code: 1 = SB transition occurrence.
-1 = Land breeze transition occurrence (not implemented).
-2 = No SB transition detected in low pass (LP) filtered signal.
-3 = Multiple SB transitions detected in band pass (BP) filtered signal.
-4 = SB time difference in LP and BP exceeds 6 hours.

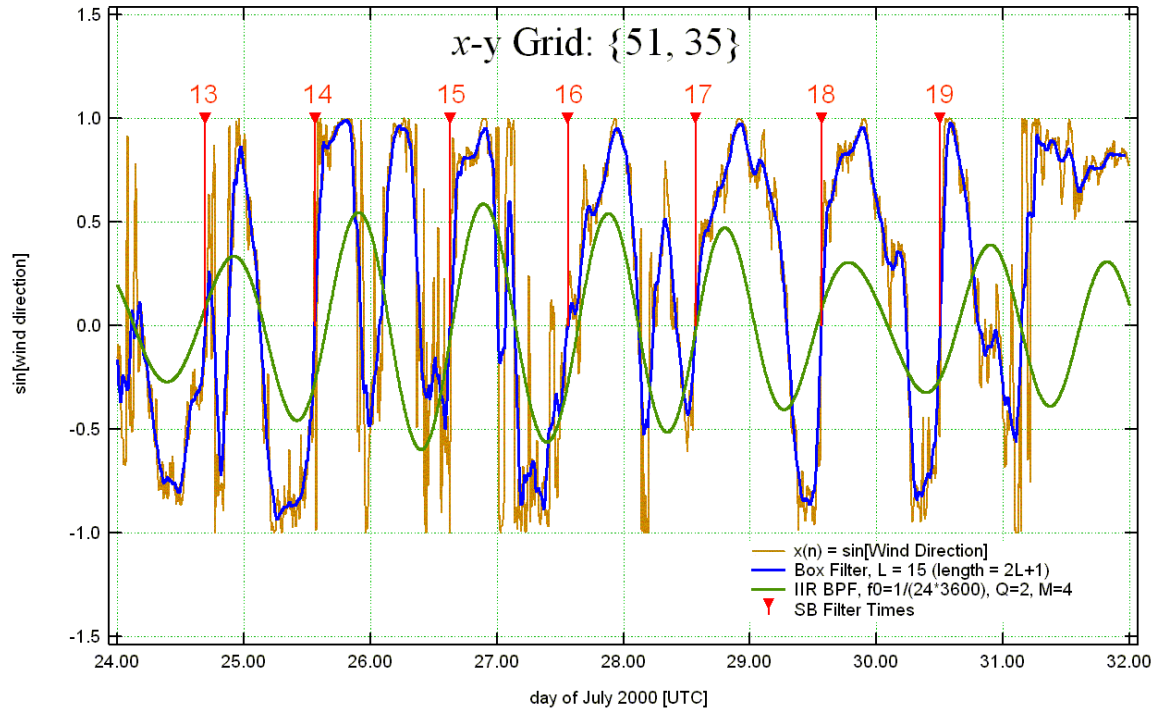


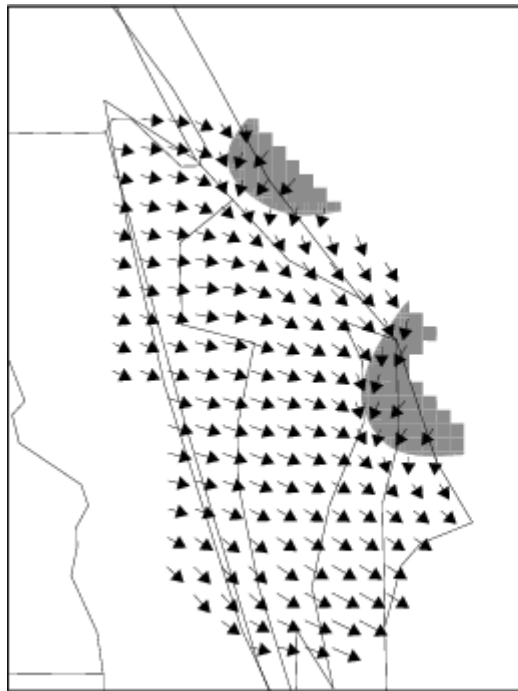
Figure 6. Results of SB filter from Figure 4, applied to wind direction data from 24–31 July 2000. Red sticks indicate the estimated SB transition times derived from the IIR BP filter (BPF) and LP filter.

3.3 Sample Output from 18 July 2000

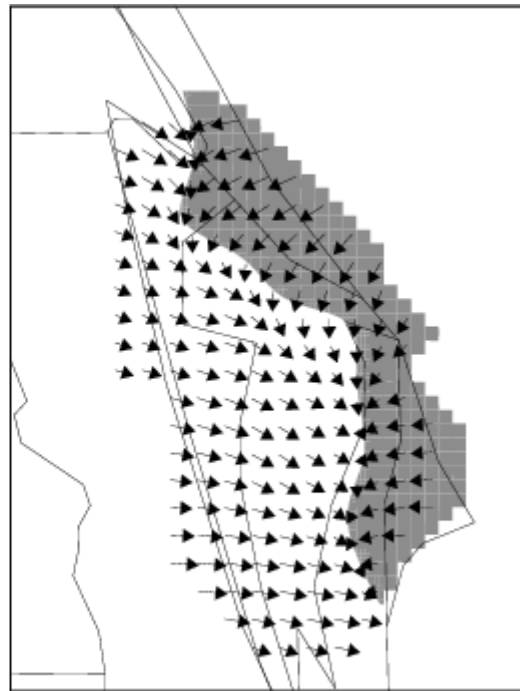
This sub-section presents sample CEM output from 18 July 2000, illustrating a day with a typical SB passage in both the observed and forecast wind fields. Figure 7 depicts an hourly sequence of the observed 54-ft wind field on 18 July from 1600 to 1900 UTC. Northwesterly winds are prevalent across much of the domain at 1600 UTC, with only a small portion of the grid near the coast experiencing onshore winds from the northeast (indicated by shading in Fig. 7a). By 1700 UTC, east-northeast winds have advanced inland along the entire eastern portion of the domain (Fig. 7b). Over the next two hours, the SB transition zone moved through much of the remainder of the domain with east-northeast winds prevailing behind the front (Figs. 7c-d).

The RAMS forecast wind fields interpolated to 54 ft (Fig. 8) are quite similar to the hourly observed winds. At 1600 UTC, only a slight shift to an easterly component occurred along the extreme eastern portion of the grid domain (Fig. 8a). Over the next three hours (Figs. 8b-d), the RAMS SB wind shift advanced inland at a very similar rate and orientation compared to the observed winds (Figs. 7b-d).

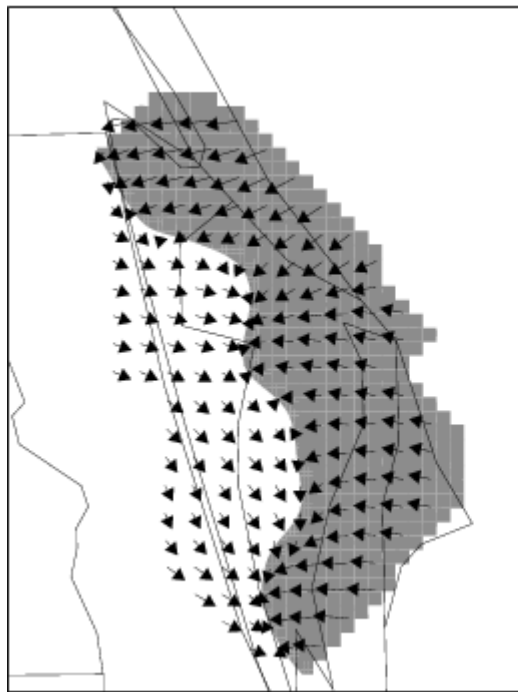
The CEM output at each grid point provides a basis for isochrones of the SB transition zone shown in Figures 9a and 9b. The RAMS isochrones of SB transition time (Fig. 9a) illustrates the steady west-southwestward progress of the SB front from about 1600 UTC to after 1900 UTC. The observed isochrone pattern in Figure 9b is quite similar with only slight deviations from the forecast pattern. Following the traditional meteorological convention in NWP model verification, the observed field is subtracted from the RAMS forecast field of SB transition times (Forecast – Observed), yielding the difference field of SB transition times in Figure 9c. Most of the SB transition time differences are less than 0.5 hours in magnitude with little indication of a systematic error across the verification domain.



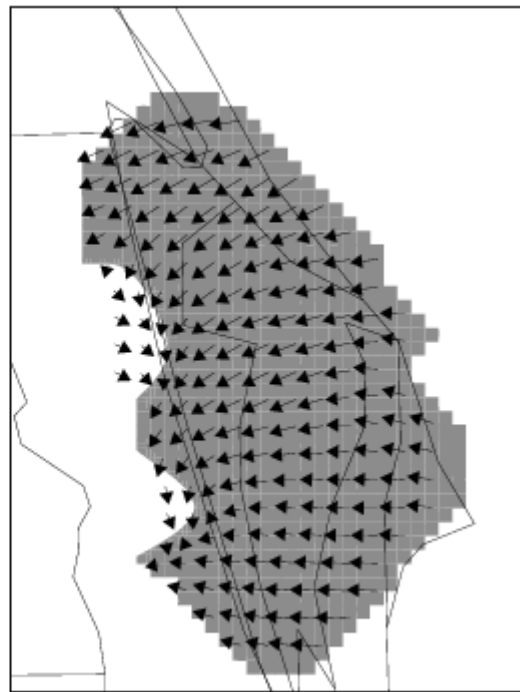
(a) Observations at 1600 UTC 18 July



(b) Observations at 1700 UTC 18 July

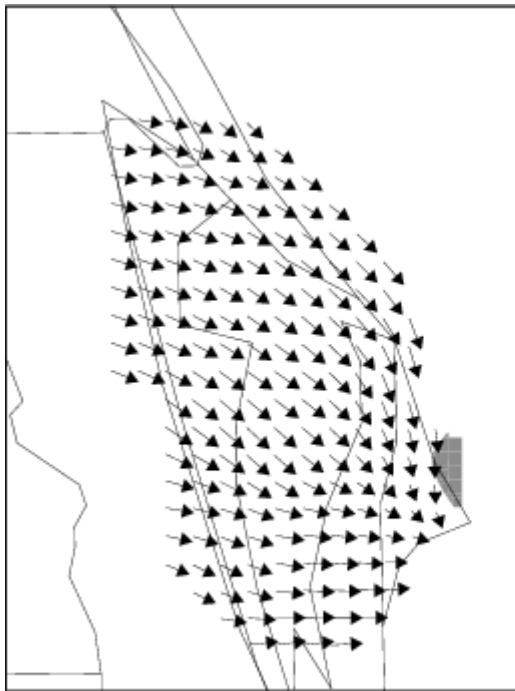


(c) Observations at 1800 UTC 18 July

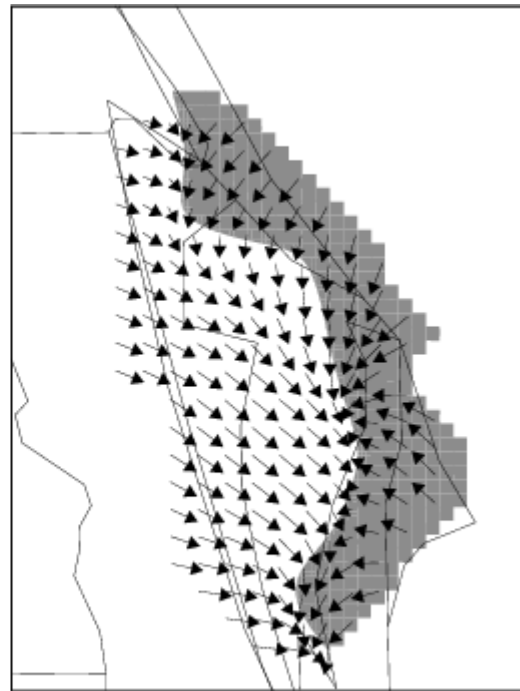


(d) Observations at 1900 UTC 18 July

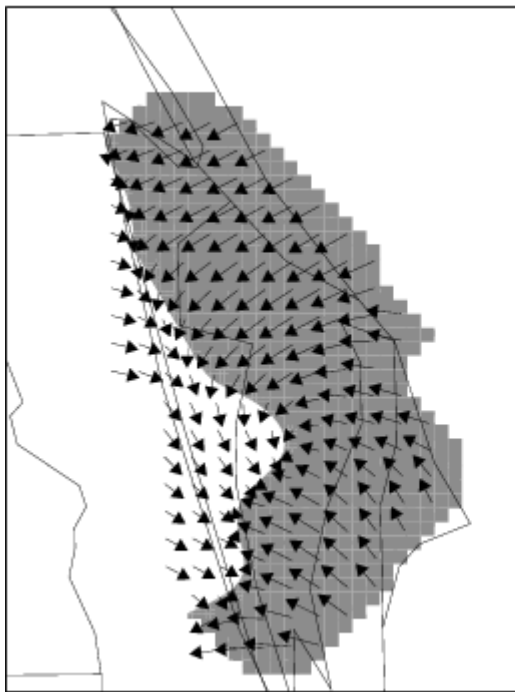
Figure 7. Hourly sequence of objectively analyzed tower winds at 54 ft, valid on 18 July 2000 at (a) 1600 UTC, (b) 1700 UTC, (c) 1800 UTC, and (d) 1900 UTC. Shading denotes areas with wind directions between 0° and 180° (i.e. onshore).



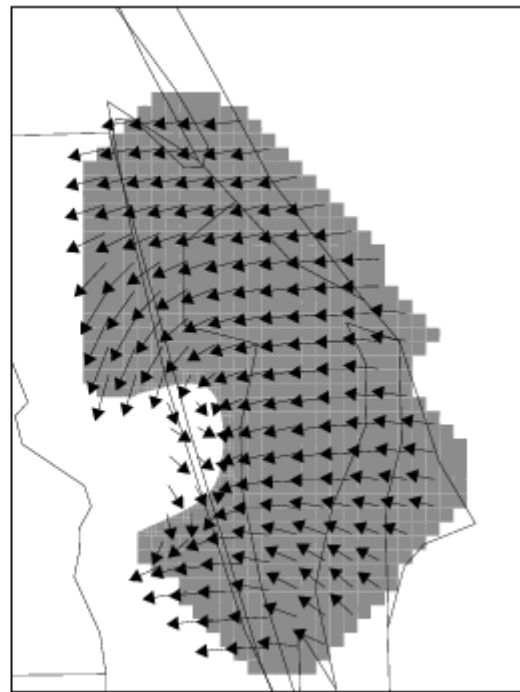
(a) 1200 UTC RAMS at 1600 UTC 18 July



(b) 1200 UTC RAMS at 1700 UTC 18 July



(c) 1200 UTC RAMS at 1800 UTC 18 July



(d) 1200 UTC RAMS at 1900 UTC 18 July

Figure 8. Hourly sequence of objectively analyzed RAMS forecast winds (interpolated to 54 ft) from the 1.25-km grid, initialized at 1200 UTC 18 July. Valid times from 18 July 2000 are (a) 1600 UTC (4-h forecast), (b) 1700 UTC (5-h forecast), (c) 1800 UTC (6-h forecast), and (d) 1900 UTC (7-h forecast). Shading denotes areas with wind directions between 0° and 180° (i.e. onshore).

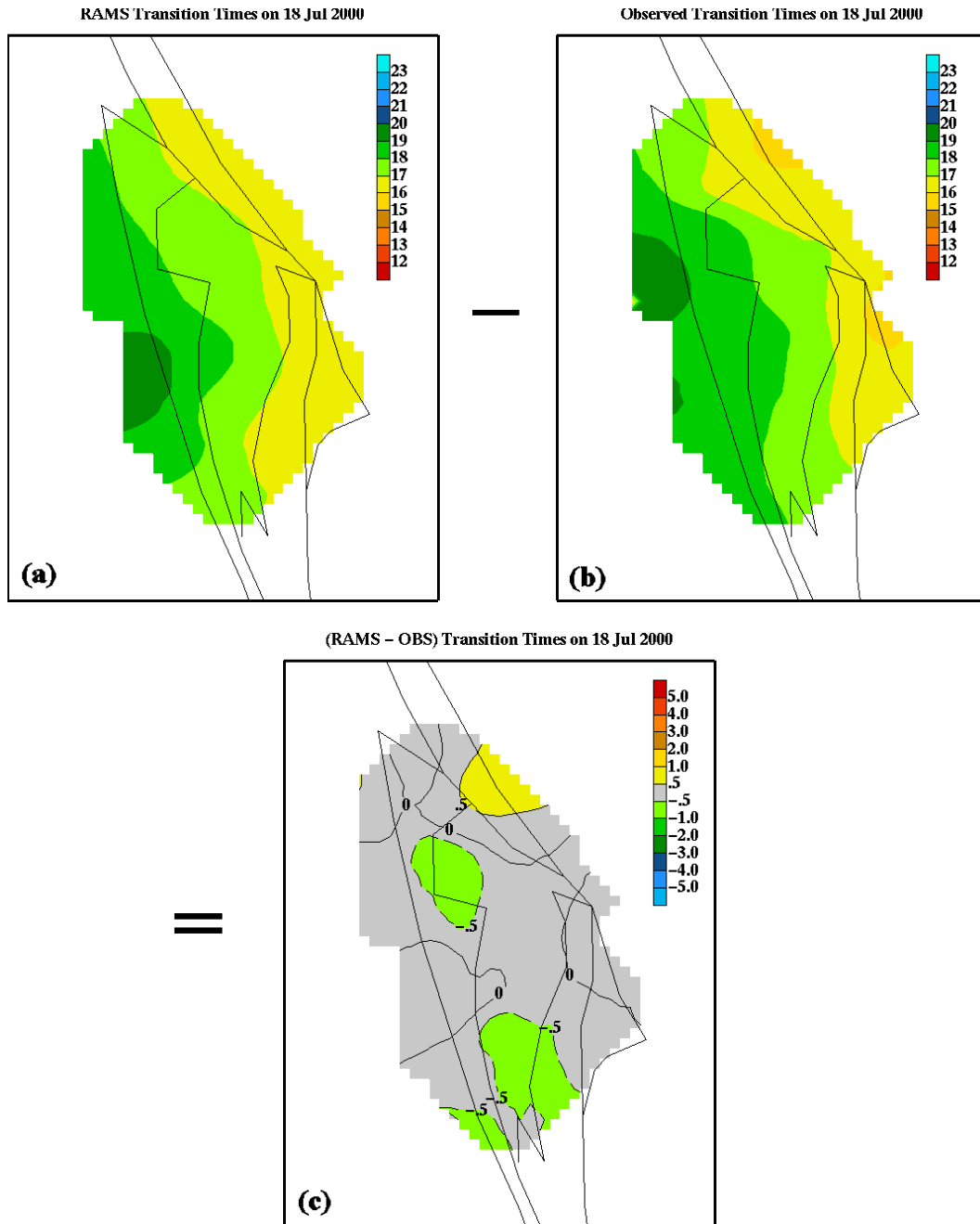


Figure 9. Sample output of the CEM algorithm for 18 July 2000. (a) RAMS forecast transition times, (b) Observed transition times, and (c) The difference in the transition times.

3.4 Image Erosion to Suppress Contamination by River Breezes

Image erosion is a common processing technique used to shrink an image object in some predictable way (Gonzalez and Woods 1992). Image erosion was used to suppress the river breeze part of the SB transition time images, using the gradient of the transition times to trigger the erosion process, as described in this section. The river breeze can often develop in advance of the actual SB transition, and move from west to east (from the Indian River to KSC/CCAFS), opposite of the direction of the SB.

The inverse of the gradient of the SB transition time is proportional to the sea-breeze boundary velocity, as depicted by Equation (2):

$$\bar{v}(x, y) = \frac{\nabla t_{SB}(x, y)}{|\nabla t_{SB}(x, y)|^2} \quad (2)$$

where $t_{SB}(x, y)$ is the SB transition time. Even though Equation (2) describes a quantitative method of computing the SB boundary velocity, the gradient of $t_{SB}(x, y)$ is a more useful quantity. If the east to west direction is taken as positive, then a positive value of $[\nabla t_{SB}(x, y)]_x = \nabla_x t_{SB} = \frac{\partial t_{SB}}{\partial x}$ indicates a SB boundary propagating from east to west.

Figure 10 illustrates such a positive SB transition and the proportionality to the propagation velocity from 12 July. Note that the gradient of the SB transition is proportional to the inverse of the SB boundary propagation velocity, as denoted in Figures 10b and 10d.

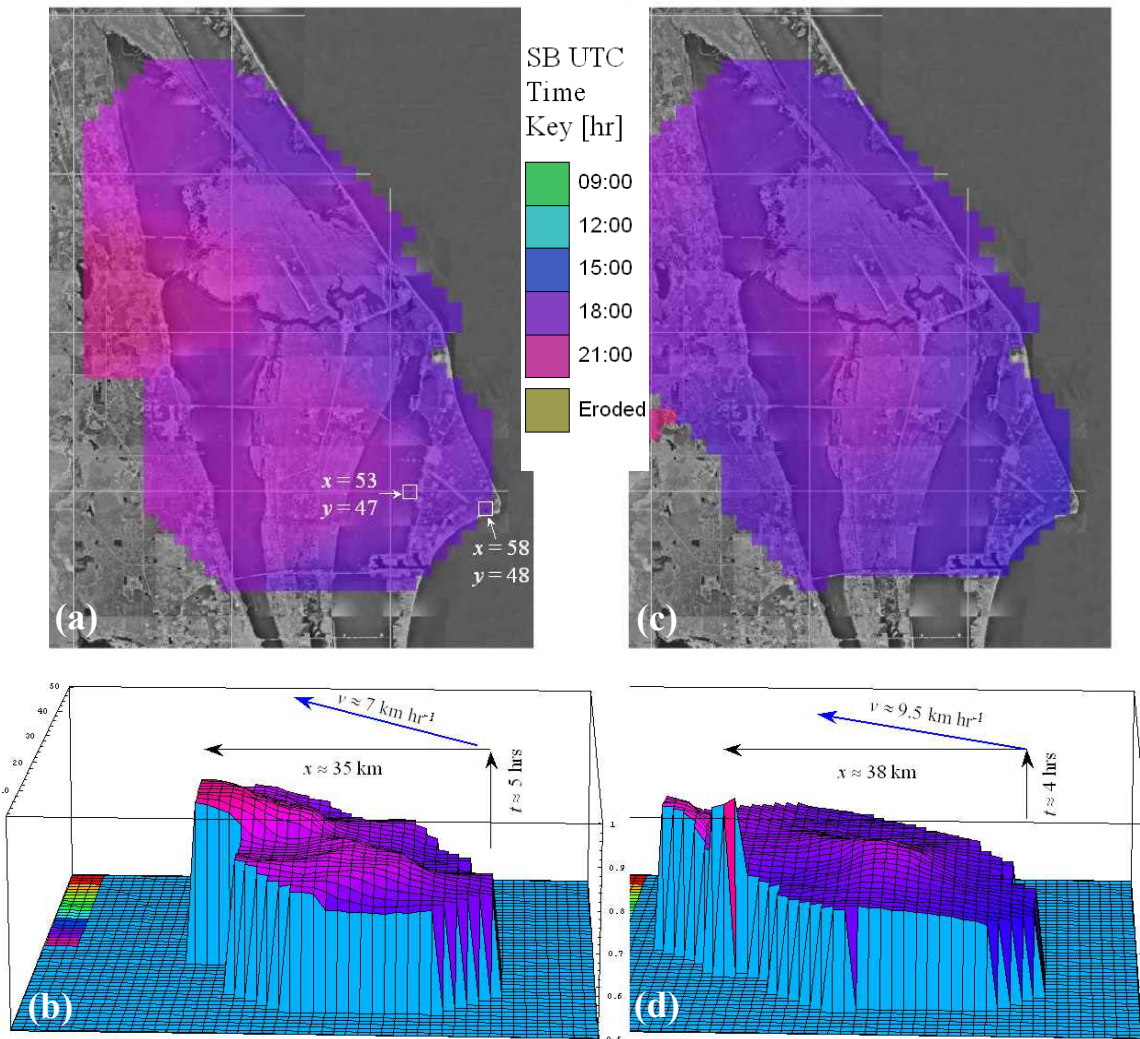


Figure 10. Sea-breeze transition times for 12 July 2000. (a) Surface plot using observed tower data, (b) Three-dimensional plot using observed data, (c) Surface plot using RAMS forecast data, and (d) Three-dimensional plot using RAMS forecast data.

However, $\nabla_x t_{SB} < 0$ indicates a west to east propagation of the wind direction boundary. Since the SB time estimation filter suppresses most effects of outflow boundaries (convective rainfall), a negative $\nabla_x t_{SB}$ is most likely indicative of a river breeze pushing the SB boundary backward. Therefore, a negative gradient of the SB transition time $\nabla_x t_{SB}$ is a strong indicator of river breeze effects. This characteristic was used to eliminate the river breeze contaminated portions of the CEM difference images, and isolate the SB transition times only. By scanning east to west, if a negative gradient was detected (i.e. a boundary moving west to east, which cannot physically be a SB transition), then all SB times to the west of that point were re-coded as no SB. This simple technique resulted in a reasonable suppression of river-breeze phenomenon which contaminated the primary SB boundary propagation. Figure 11 shows an example map of the SB transition times from 18 August 2000, before and after image erosion.

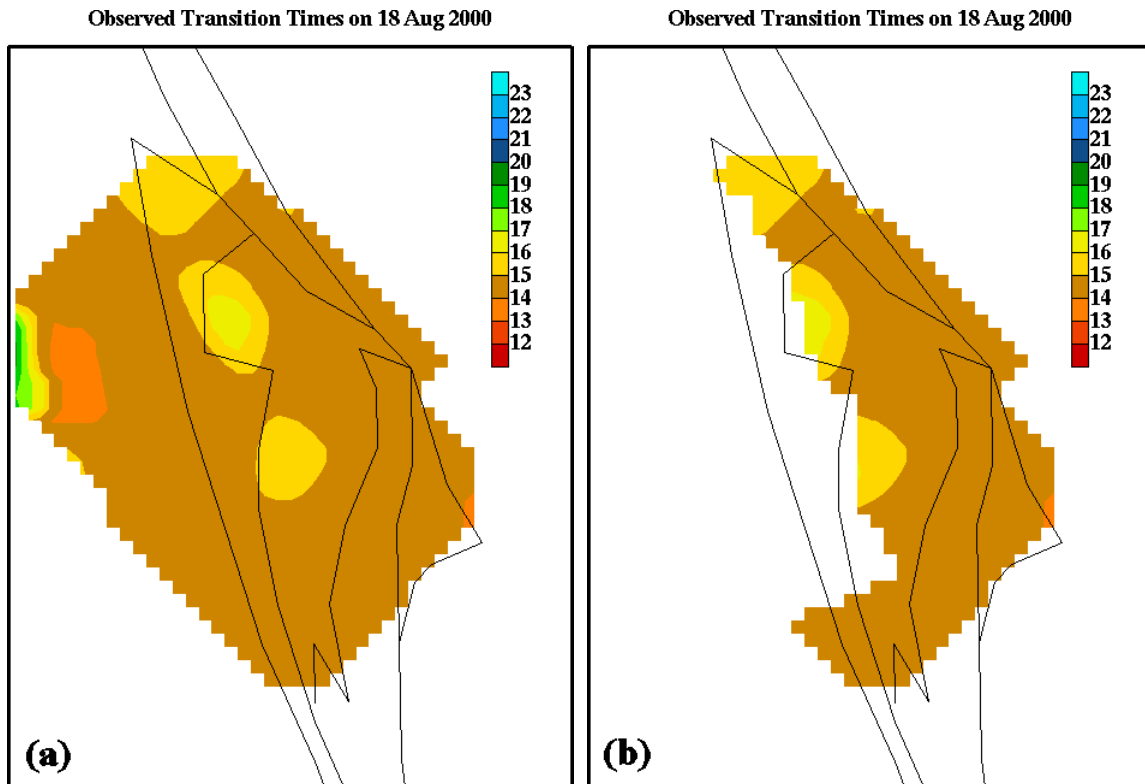


Figure 11. Erosion based on the gradient of the SB transition time of the observed wind field on 18 August 2000: (a) Before erosion, and (b) after erosion.

4. Algorithm Validation and Results

This section presents the validation of the CEM algorithm and the RAMS verification results as generated by CEM. An interpretation of the CEM output is also provided to explain the significance of the objective verification parameters.

4.1 Validation of CEM

Tables 4 and 5 summarize the results of the Gaussian fit parameters of CEM for July and August 2000, as well as present the subjectively determined SB transition time for the observed and forecast wind fields. The subjective SB transition times were determined by examining animations of 5-minute observed and RAMS forecast wind fields across KSC/CCAFS, similar to Figures 7 and 8. The range of SB transition times were identified based on the presence and continuity of a landward-propagating wind-shift line in the two-dimensional wind field, as interpreted by an experienced meteorologist.

Additional archived data sources such as radar and satellite observations were also examined for each day to ensure that no precipitation outflow boundaries caused the landward-moving wind-shift line. The beginning and end times of the SB transition time ranges were recorded based on the first and last appearance of the landward-moving wind shift within the tower analysis domain. The presence of precipitation outflow boundaries and river breezes in the observed and forecast wind fields were noted during the analysis.

The CEM technique performed quite well when compared to these subjective meteorological assessments of the SB transition times. The algorithm correctly identified a forecast or observed SB occurrence or absence 93% of the time during the two-month evaluation period from July and August 2000. Given the 104 possible validation events (52 days with non-missing data for both observed and forecast data), there were 97 successes and only 7 failures in identifying the correct SB occurrence or absence. All failures and their explanations are indicated by a footnote in either the f_O or f_R column of Tables 4 and 5. Six of the 7 failures were caused by precipitation outflow boundaries that generated easterly flow, resulting in a false identification of a SB occurrence (July 7, 15, 16, 30, and August 22). The only CEM missed identification of a SB occurrence is found on July 17, when the observed SB transition briefly affected only the extreme eastern portion of the verification domain.

The CEM could be improved to recognize areas of precipitation by incorporating additional data sources such as radar reflectivity and model-predicted rainfall rates. Image processing techniques could be used to denote areas of observed or forecast precipitation in relation to the transition times identified by CEM. The incorporation of these additional data sources is beyond the scope of the current effort; however, CEM could be improved by introducing more sophistication to account for wind transition zones associated with precipitation features.

A qualitative comparison between the CEM timing errors and the subjectively determined observed and forecast transition times indicate that the algorithm performed very well overall. In most instances, the mean SB transition time bias (τ) is comparable to the difference between the subjectively determined RAMS and observed transition times (Forecast – Observed). However, differences could occur due to the specific positioning and orientation of the observed versus forecast SB transition zone, which cannot be adequately depicted by the subjectively determined time ranges.

Most substantial discrepancies between the CEM bias results and the subjective time ranges were again caused by observed or forecast areas of precipitation that led to complex wind patterns not handled well by CEM. Out of the 35 days correctly identified by CEM for comparison between observed and forecast SB transition times, only 4 days had substantial discrepancies between the subjectively determined RAMS and observed sea breeze times and the CEM bias (τ): July 13 and 26, and August 2 and 6. Once again, 3 out of 4 of these discrepancies were caused by either observed or forecast precipitation outflow that contaminated the wind fields. The fourth discrepancy (2 August) was caused by prevailing onshore flow in RAMS near the initialization time, which led to a prematurely early identification of the SB transition time in the model and thus, an erroneously large early (negative) bias.

Table 4. Gaussian fit parameters for eroded CEM histograms and subjectively-determined range of observed and RAMS times of the SB transition (in UTC) for July 2000. The parameters shown are the mean SB transition time bias (τ), the standard deviation of the SB transition differences (σ), the fractional area of the domain with only an observed SB transition (f_o), and the fractional area of the domain with only a RAMS forecast SB transition (f_R). Erroneous identifications of a SB occurrence/absence and inconsistent biases are indicated by shaded cells, along with a footnote explaining the reason(s) for the discrepancy.

Day	τ (hours)	σ (hours)	f_o	f_R	Observed SB Times	RAMS SB Times
2			0	0	None	None
3			0	0	None	None
4			0	0	None	None
5	-0.01	1.47	0.69	0.21	1300-1600	1330-1500
6	-0.90	0.54	0.16	0.07	1715-2145	1700-1830
7			0	1 ^A	None	None
8	-0.93	0.22	0.01	0.03	1545-1645	1430-1600
9			0	0	None	None
10			0	0	None	None
11	0.22	0.48	0.02	0.38	1430-1700	1525-1700
12	-0.31	0.46	0.21	0.10	1600-2015	1700-1830
13	-2.44	0.05	0	0.97	1715-1815 ^B	1710-2145
14			0	1	None	1700-2355
15			0	1 ^A	None	None
16			0	1 ^A	None	None
17			0 ^C	0	2045-2215 ^C	None
18	-0.12	0.35	0.01	0	1600-1900	1600-1930
19	0.29	0.28	0.32	0.03	1330-1500	1330-1600
20	-3.61	0.65	0.23	0.14	1740-2355	1515-1745
21	-1.69	0.45	0.05	0.42	1630-2030	1530-1930
22	-1.16	0.55	0.09	0.50	1645-1900	1615-2000
23	-1.09	0.39	0.05	0.18	1545-1800	1500-1945
24	-0.69	1.04	0.13	0.27	1430-1730	1430-1915
25	-2.08	1.24	0.52	0.06	1430-1745	1400-1515
26	-0.51	1.86	0.42	0.24	1515-1845	1345-1500 ^D
27	-1.23	0.30	0.87	0	1315-1650	1330-1530
28	-0.94	0.23	0.09	0.40	1330-1530	1300-1400
29	-0.69	0.42	0.14	0.01	1315-1600	1330-1500
30	-0.02	0.21	0.30 ^A	0.05 ^A	None	None

^ACEM falsely identified a model SB due to precipitation outflow with an easterly wind component.

^BThe observed SB ended prematurely due to precipitation outflow.

^CThe observed SB occurred only at the extreme eastern tip of the grid domain under strong westerly flow.

^DThe RAMS SB times ended prematurely due to contamination from forecast precipitation outflow.

Table 5. Gaussian fit parameters for eroded CEM histograms, and subjectively-determined range of observed and RAMS times of the SB transition (in UTC) for August 2000. The parameters shown are the mean SB transition time bias (τ), the standard deviation of the SB transition differences (σ), the fractional area of the domain with only an observed SB transition (f_o), and the fractional area of the domain with only a RAMS forecast SB transition (f_R).

Day	τ (hours)	σ (hours)	f_o	f_R	Observed SB Times	RAMS SB Times
2	-3.63 ^A	0.29	0.37	0	1430-1530	1400-1600
3	-0.49	0.46	0.20	0.42	1345-1445	1300-1415
4	-0.12	0.96	0.16	0.56	1500-1700	1510-1700
5	-1.99	0.75	0.13	0.07	1715-1900	1515-1740
6	1.36	0.74	0.17	0.30	1330-1600	1330-1500 ^B
7			1	0	1330-1430	None
8					1300-1400	Missing Data
9	-0.05	0.23	0.17	0.03	1300-1500	1330-1550
10	-0.13	0.67	0.06	0.48	1515-1800	1500-1820
11					1730-1900	Missing Data
12					None	Missing Data
13					None	Missing Data
14					None	Missing Data
15					1445-1730	Missing Data
16	0.74	0.42	0.19	0.19	1300-1500	1330-1600
17	1.25	0.56	0.54	0.16	1300-1600	1330-1630
18	0.38	0.29	0.10	0.04	1415-1530	1400-1610
19	0.17	0.50	0.15	0.25	1530-1645	1530-1700
20	-0.15	0.43	0.14	0.16	1500-1630	1500-1700
21	-0.12	0.18	0.05	0.06	1400-1515	1345-1530
22			1 ^C	0	None	None
23			0	0	None	None
24			0	0	None	None
25	-0.68	0.61	0.04	0.30	1500-1730	1400-1700
26	-0.72	0.56	0.21	0.12	1400-1715	1400-1520
27			1	0	1315-1500	None
28	-1.76	0.35	0.08	0.24	1400-1730	1400-1515
29	-4.82	0.21	0.14	0.23	1800-2030	1400-1500
30	-2.04	0.49	0.50	0	1700-2230	1515-1930

^AModel flow was slightly onshore at model initialization time, thus identifying the forecast SB too early.

^BThe RAMS SB times ended prematurely due to contamination from forecast precipitation outflow.

^CPrecipitation outflow caused easterly flow that triggered a false identification of an observed SB.

4.2 Interpreting Objective Model Verification Results

Tables 4 and 5 summarize the Gaussian fit parameter statistics for each day during July and August 2000 with both an observed and forecast SB. Zeros in the same row under both f_O and f_R in Tables 4 and 5 indicate that neither a forecast nor observed SB occurred on that day (representing a forecast success). Blank rows indicate that forecast and/or observed data were missing for that day. A complete forecast miss or false prediction of a SB on a particular day is represented by a value of unity for f_O (forecast failure) or f_R (false alarm prediction).

The days with the best model skill in predicting the SB occurrence and timing are those with the smallest absolute values of the mean bias (τ) and the smallest standard deviation of the bias (σ). Days that have a larger absolute value of τ indicate the greatest systematic timing errors in RAMS. Note that an average early bias in the onset of the SB transition on a particular day is given by a negative τ , whereas a positive τ indicates a late bias in the onset of the SB transition.

The standard deviation (σ) denotes the amount of variation in the SB transition time error across the KSC/CCAFS grid domain. If the overall timing bias τ is small, the RAMS SB forecast could still be in substantial error over portions of the domain due to a large σ . In these instances, a large σ combined with a nearly unbiased τ would indicate that the RAMS forecast SB had a phase error or did not propagate in the correct manner. For example, the forecast SB could start too late along the coastal regions and then propagate too quickly across KSC/CCAFS reaching the western portion of the domain too early. Such a scenario would yield a nearly unbiased domain-wide timing error τ , but would also yield a relatively large σ , due to the variation of the timing errors across the domain.

Based on the results of CEM in Tables 4 and 5, RAMS tended to predict the onset and movement of the SB transition too early and/or quickly. The domain-wide timing biases provided by CEM indicated an early bias on 30 out of 37 days when both an observed and forecast sea breeze occurred over the same portions of the analysis domain. These results are fairly consistent with a previous subjective verification of the RAMS sea breeze predictions conducted during the same time of year (Case et al. 2002). In the Case et al. (2002) subjective verification, 12 towers were selected and examined daily for SB transitions during the 1999 and 2000 summer months. They found that RAMS had about a 0.3 h early (negative) timing bias in the SB onset at those 12 selected towers. However, these results cannot be directly compared to the CEM results since the current study takes into account all available KSC/CCAFS towers, and only compares the SB times during July and August 2000.

To summarize, the CEM results are more valuable than the subjective evaluation results for two reasons:

- All available observational and RAMS point forecast data are utilized in the verification, and
- CEM is fully automated, saving considerable manpower compared to a subjective analysis.

4.3 Mean Post-Sea Breeze Wind Comparisons

Using eroded SB transition times, the average of wind speed and direction for all days with detected SB passage during July and August 2000 are shown in Figure 12. Comparing the observed to forecast data, it can be seen that the post-SB wind direction is better predicted by RAMS than the post-SB wind speeds. The overall wind-speed bias for all valid days shown in Figure 8 is 2.0 m s^{-1} with an error standard deviation of 1.2 m s^{-1} . Out of the 38 events shown in Figures 8a-b, all days experienced stronger post-SB winds in the model compared to observations. Meanwhile for wind direction, the overall bias is only 9° with an error standard deviation of 26° , indicating that the post-SB forecast wind direction is relatively unbiased.

It is important to note that out of the 37 SB events with comparison Gaussian statistics in Tables 4 and 5, 30 of these events had a negative τ , or early timing biases in RAMS. An early model timing bias in the SB transition could be caused by a number of factors in the model; however, in all SB events, RAMS over-predicted the strength of the post-SB wind speeds (Figures 12a-b). Therefore, it appears that some aspect of RAMS leads to a consistent over-prediction of the wind speeds behind the SB front, often resulting in an early bias in the onset time of the SB.

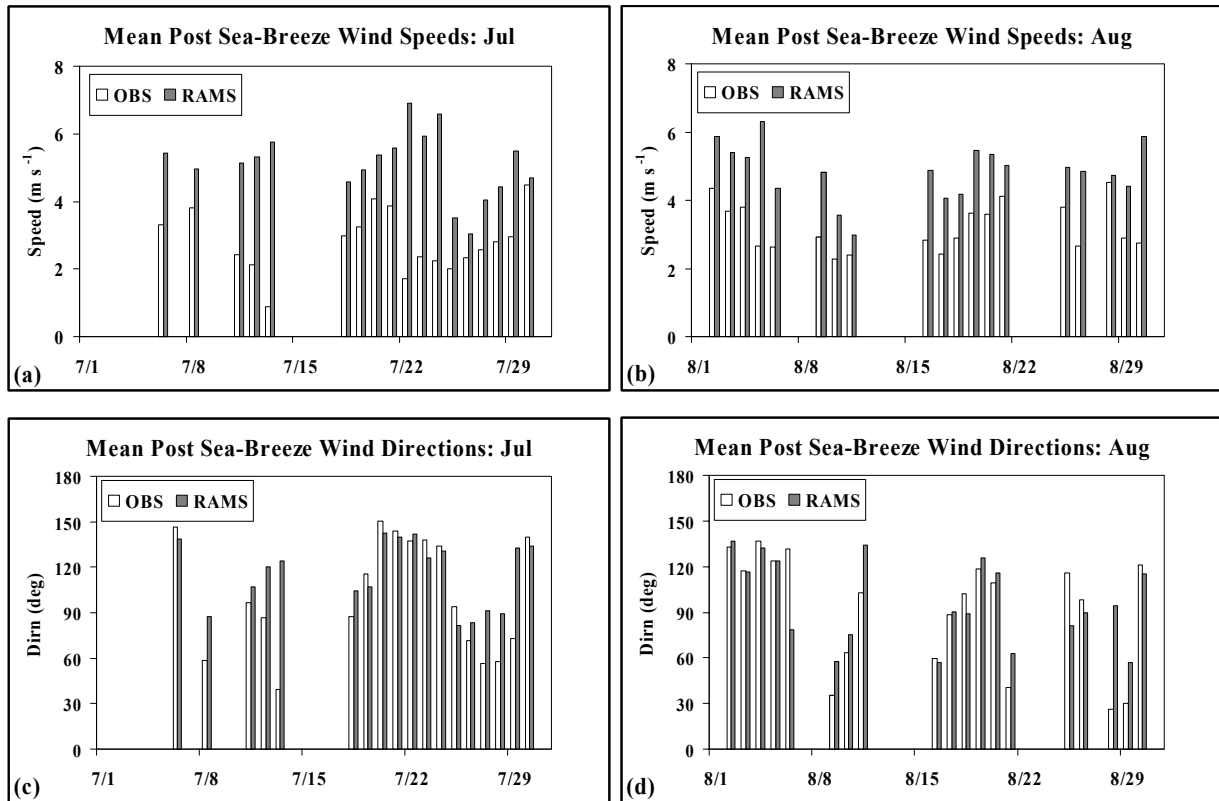


Figure 12. Mean post-SB winds based on eroded SB transition times: (a) Mean wind speeds for July 2000, (b) Mean wind speed for August 2000, (c) Mean wind direction for July 2000, and (d) Mean wind direction for August 2000.

5. Summary

This report presented the CEM objective technique to verify RAMS predictions of the SB phenomenon over east-central Florida. The CEM technique identifies SB transition times in objectively-analyzed grids of observed and forecast wind, verifies the RAMS SB transition times against the observed times, and computes the mean post-sea breeze wind direction and speed to compare the observed and forecast winds behind the SB front.

The CEM technique is superior to traditional objective verification techniques and previously-used subjective verification methodologies because:

- It is automated, requiring little manual intervention,
- It accounts for both spatial and temporal scales and variations,
- It accurately identifies and verifies the sea-breeze transition times, and
- It provides verification contour maps and simple statistical parameters for easy interpretation.

The CEM uses a parallel lowpass boxcar filter and a high-order bandpass filter to identify the SB transition times in the observed and RAMS grid points. Once the transition times are identified, CEM fits a Gaussian histogram function to the actual histogram of transition time differences between the model and observations. The fitted parameters of the Gaussian function subsequently explain the timing bias and variance of the timing differences across the valid comparison domain. Once the transition times are all identified at each grid point, the CEM then computes the mean wind direction and speed during the remainder of the day for all times and grid points after the SB transition time. The mean post-SB RAMS winds were then compared to the mean post-SB observed winds.

The CEM technique performed quite well when compared to a subjective assessments of the SB transition times. The algorithm correctly identified a forecast or observed SB occurrence or absence 93% of the time during the two-month evaluation period. Nearly all failures in CEM were the result of complex precipitation features (observed or forecast) that contaminated the wind field, resulting in a false identification of a SB transition.

A qualitative comparison between the CEM timing errors and the subjectively determined observed and forecast transition times indicates that the algorithm performed very well overall. Most discrepancies between the CEM results and the subjective analysis were again caused by observed or forecast areas of precipitation that led to a contaminated SB signal. The CEM also failed on a day when the observed SB transition affected only a very small portion of the verification domain.

Based on the results of CEM, the RAMS tended to predict the onset and movement of the sea-breeze transition too early and/or quickly. The domain-wide timing biases provided by CEM indicated an early bias on 30 out of 37 days when both an observed and forecast SB occurred over the same portions of the analysis domain. A comparison of the mean post-SB winds indicate that RAMS has a positive wind-speed bias for all days, consistent with the early bias in the SB transition time.

Objective error statistics for specific meteorological phenomena, such as those developed in this project for the SB, can provide forecasters and model developers with an important tool in diagnosing model biases or errors. The potential savings in time and resources, combined with the knowledge gained from such an evaluation could prove invaluable for future development of mesoscale NWP models.

6. References

- Atkinson, B. W., 1981: Sea/Land Breeze Circulation. *Mesoscale Atmospheric Circulations*, Academic Press, 125-214.
- Baldwin, M. E., S. Lakshmiarahan, and J. S. Kain, 2001: Verification of mesoscale features in NWP models. Preprints, *Ninth Conf. on Mesoscale Processes*, Ft. Lauderdale, FL, Amer. Meteor. Soc., 255-258.
- Baldwin, M. E., S. Lakshmiarahan, and J. S. Kain, 2002: Development of an “events-oriented” approach to forecast verification. Preprints, *19th Conf. on Weather Analysis and Forecasting and 15th Conf. on Numerical Weather Prediction*, San Antonio, TX, Amer. Meteor. Soc., 210-213.
- Barnes, S. L., 1964: A technique for maximizing details in numerical weather map analysis. *J. Appl. Meteor.*, **3**, 396-409.
- Benjamin, S. G., and Coauthors, 1998: The operational RUC-2. Preprints, *16th Conf. on Weather Analysis and Forecasting*, Phoenix, AZ, Amer. Meteor. Soc., 249-252.
- Case, J. L., J. Manobianco, A. V. Dianic, M. M. Wheeler, D. E. Harms, and C. R. Parks, 2002: Verification of high-resolution RAMS forecasts over east-central Florida during the 1999 and 2000 summer month. *Wea. Forecasting*, **17**, 1133-1151.
- Chen, S., and W. R. Cotton, 1988: The sensitivity of a simulated extratropical mesoscale convective system to longwave radiation and ice-phase microphysics. *J. Atmos. Sci.*, **45**, 3897-3910.
- Cotton, W. R., M. A. Stephens, T. Nehr Korn, and G. J. Tripoli, 1982: The Colorado State University three-dimensional cloud/mesoscale model — 1982. Part II: An ice phase parameterization. *J. Rech. Atmos.*, **16**, 295-320.
- Gonzalez, R. C. and R. E. Woods, 1992: Digital Image Processing. Addison-Wesley Publishing Company, 716 pp.
- Hillman, G. D. and J. E. Lane, 1989: Real-time determination of IIR coefficients for cascaded butterworth filters. *IEEE Intl. Conf. On Acoustics Speech and Signaling Processing*, Glasgow, Scotland, 1353-1356.
- Manobianco, J., and P. A. Nutter, 1999: Evaluation of the 29-km Eta Model. Part II: Subjective verification over Florida. *Wea. Forecasting*, **14**, 18-37.
- Mellor, G. L., and T. Yamada, 1982: Development of a turbulence closure model for geophysical fluid problems. *Rev. Geophys. Space Phys.*, **20**, 851-875.
- Nutter, P. A., and J. Manobianco, 1999: Evaluation of the 29-km Eta Model: Part I: Objective verification at three selected stations. *Wea. Forecasting*, **14**, 5-17.
- Pielke, R. A., and Coauthors, 1992: A comprehensive meteorological modeling system — RAMS. *Meteor. Atmos. Phys.*, **49**, 69-91.
- Rabiner, L. R. and B. Gold, 1975: Theory and Application of Digital Signal Processing. Englewood Cliffs, NJ, Prentice-Hall, 752 pp.
- Tremback, C. J., 1990: Numerical simulation of a mesoscale convective complex: Model development and numerical results. Ph.D. dissertation, Atmos. Sci. Paper No. 465, Department of Atmospheric Science, Colorado State University, Fort Collins, CO 80523, 247 pp.
- Tremback, C. J., and R. Kessler, 1985: A surface temperature and moisture parameterization for use in mesoscale numerical models. Preprints, *Seventh Conf. on Numerical Weather Prediction*, Montreal, Quebec, Amer. Meteor. Soc., 355-358.

Appendix A: Gradient Search Method to Fit Gaussian Probability Function

A histogram h_k of difference times can be generated from a CEM spatial plot. The sample histogram of Figure A1 is generated by summing the number of occurrences of times corresponding to the k th time difference, using all pixels in the image which have a defined CEM difference time.

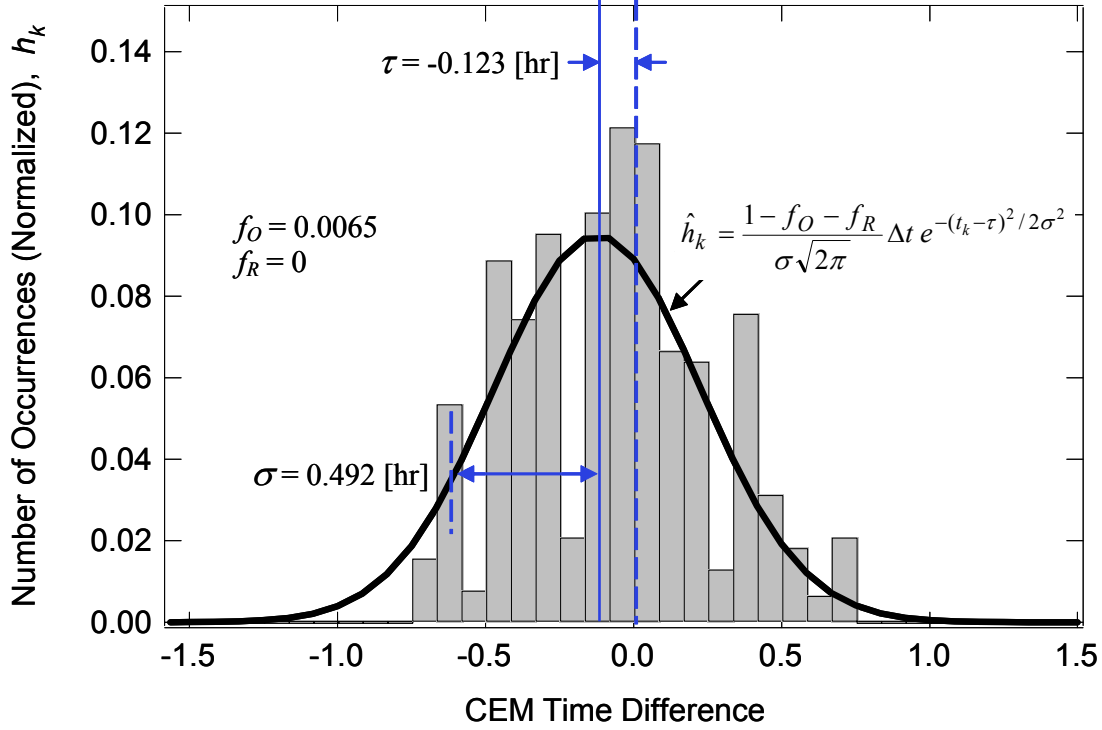


Figure A1. Sample CEM histogram showing Gaussian fit from equation (A1).

The histogram h_k can be approximated by a Gaussian probability function $\hat{h}_k \equiv \hat{h}(t_k)$, where $t_k \equiv k\Delta t$:

$$\hat{h}_k = \frac{1 - f_O - f_R}{\sigma\sqrt{2\pi}} \Delta t e^{-(t_k - \tau)^2 / 2\sigma^2} \quad (\text{A1})$$

Equation (A1) is plotted in Figure A1 using a “best fit” set of values for τ and σ . A method to find a best fit set of values is based on the *gradient search* algorithm.

The gradient search method starts by specifying the total error defined by the sum of the squares of differences between calculated and actual values of the histogram, summed over all k points:

$$E = \sum_{k=1}^N (h_k - \hat{h}_k)^2 \quad (\text{A2})$$

In the particular case of CEM histograms used in this study, the total number of points N is equal to 288, the number of 5 min (Δt) intervals in a 24-h period. The next step in the gradient search method is to set the gradient of the total error, from Equation (A2), to zero:

$$\nabla E = 0 . \quad (\text{A3})$$

The gradient of E can be written as:

$$\nabla E = -2 \sum_{k=1}^N (h_k - \hat{h}_k) \tilde{\alpha}_k , \quad (\text{A4})$$

where

$$\tilde{\alpha}_k = \begin{bmatrix} \frac{\partial}{\partial \tau} \\ \frac{\partial}{\partial \sigma} \end{bmatrix} \hat{h}_k = \begin{bmatrix} \alpha_\tau \\ \alpha_\sigma \end{bmatrix}_k , \quad (\text{A5})$$

$$\alpha_\tau = \frac{(1 - f_O - f_R)}{\sigma^3 \sqrt{2\pi}} (t - \tau) \Delta t e^{-(t-\tau)^2 / 2\sigma^2} , \text{ and} \quad (\text{A6})$$

$$\alpha_\sigma = \frac{(1 - f_O - f_R)}{\sigma^4 \sqrt{2\pi}} [2(t - \tau)^2 - \sigma^2] \Delta t e^{-(t-\tau)^2 / 2\sigma^2} . \quad (\text{A7})$$

The parameter vector, \bar{P} whose components are the Gaussian variables, τ and σ :

$$\bar{P} = \begin{bmatrix} \tau \\ \sigma \end{bmatrix} , \quad (\text{A8})$$

are found using an iterative process described by the following formula

$$\bar{P}(n+1) = \bar{P}(n) - \mu \nabla E . \quad (\text{A9})$$

The convergent constant μ is determined empirically. If μ is too small, convergence will require an unreasonably large number of iterations of Equation (A9). If μ is too large, Equation (A9) will diverge, usually towards infinity, or oscillate wildly around the solution. In this study, a value of $0.1 < \mu < 1$ seemed to produce satisfactory results.

Appendix B: Band Pass Filter Details

As shown in Figure B1 and B2, a digital N th order bandpass filter can be implemented by cascading the second order network, where the second order transfer function for each of the M cascaded sections is expressed as:

$$H_i(z) = \frac{\alpha_i (1 - z^{-2})}{\frac{1}{2} - \gamma_i z^{-1} + \beta_i z^{-2}}. \quad (\text{B1})$$

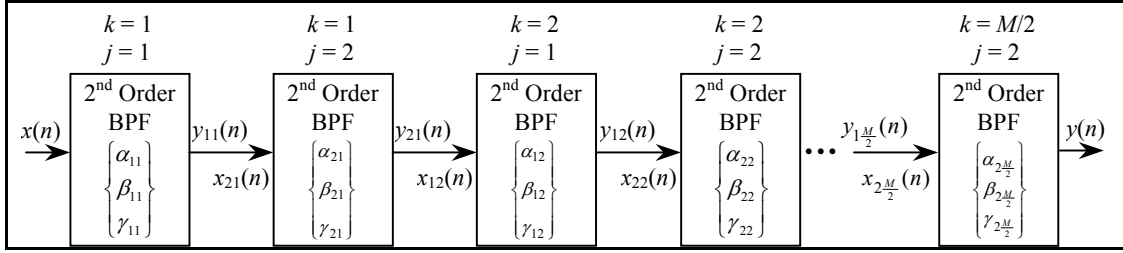


Figure B1. Cascaded N th order IIR bandpass filter network.

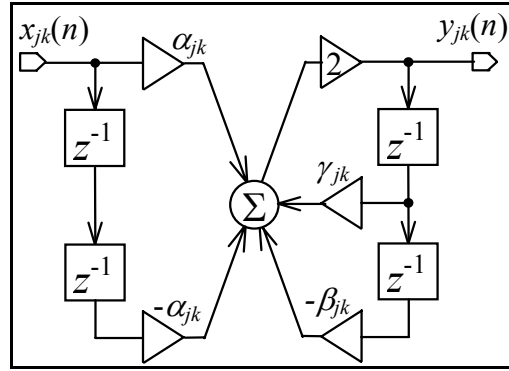


Figure B2. Single second order section of cascaded bandpass filter network.

The total transfer function $H(z)$ is the product of the M cascaded sections, where the filter order $N = 2M$:

$$H(z) = H_1(z) H_2(z) \cdots H_M(z). \quad (\text{B2a})$$

Instead of a product of M sections as described above, the network can be expressed as $M/2$ pairs of cascaded sections:

$$\begin{aligned} H(z) &= H_{11}(z) H_{21}(z) H_{12}(z) H_{22}(z) \cdots H_{1\frac{M}{2}}(z) H_{2\frac{M}{2}}(z) \\ &= \prod_{k=1}^{M/2} \prod_{j=1}^2 H_{jk}(z) = \prod_{k=1}^{M/2} \prod_{j=1}^2 \frac{\alpha_{jk} (1 - z^{-2})}{\frac{1}{2} - \gamma_{jk} z^{-1} + \beta_{jk} z^{-2}}. \end{aligned} \quad (\text{B2b})$$

The number of product terms in Equation (B2b) is still M , but now each pair of $j = 1, 2$ products correspond to a $k = 1, 2, \dots, M/2$ grouping. The reason for this organization of $H(z)$ may be more obvious by examining Figure B2: $j = 1$ corresponds to a second order bandpass filter whose center frequency is below f_0 , while $j = 2$ corresponds to a bandpass whose center frequency is above f_0 . Each pair of k sections has a gain value different than one, which is shared by both the $j = 1$ and $j = 2$ sections. This arrangement leads to a *maximally flat* bandpass design (also known as the *Butterworth* design).

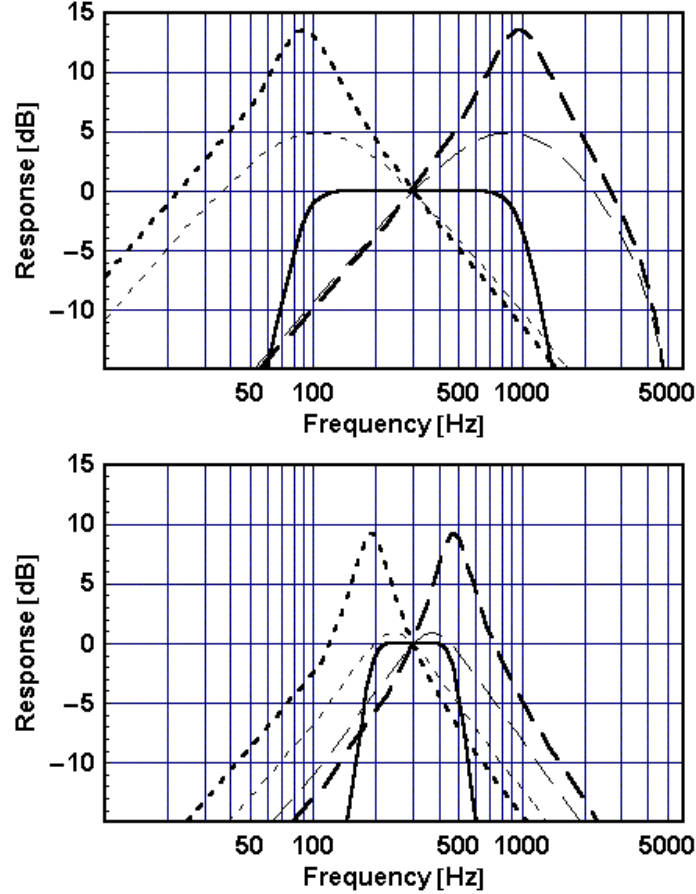


Figure B3. Gain response of 8th Order ($M=4$) Butterworth bandpass filter, showing equivalent gain response of each individual second order section for $f_0=300$ Hz and $Q=0.33$ (top), and $Q=1.0$ (bottom). The solid line is total $H(z)$, the dotted line is $H_{11}(z)$, the dashed line is $H_{21}(z)$, the thin dotted line is $H_{12}(z)$, and the thin dashed line is $H_{22}(z)$.

The coefficients α_{jk} , β_{jk} , and γ_{jk} in Equation (B2b) are directly related to the filter Q and center frequency f_0 of the total network. However, unlike the coefficient formulas of the lowpass and highpass cascaded Butterworth filters, the cascaded bandpass coefficient formulas are somewhat elaborate:

$$\beta_{jk} = \frac{1}{2} \frac{1 - \frac{1}{2} d_k \sin \theta_{jk}}{1 + \frac{1}{2} d_k \sin \theta_{jk}}, \quad (\text{B3})$$

$$\gamma_{jk} = \left(\frac{1}{2} + \beta_{jk} \right) \cos \theta_{jk}, \quad (\text{B4})$$

$$\alpha_{jk} = \frac{1}{2} \left(\frac{1}{2} - \beta_{jk} \right) \sqrt{1 + \left(\frac{W_k - 1/W_k}{d_k} \right)^2}, \quad (\text{B5})$$

$$d_k = \sqrt{\frac{d_E D_k}{A_k + \sqrt{A_k^2 - 1}}}, \quad (\text{B6})$$

$$d_E = \frac{2 \tan\left(\frac{\theta_0}{2Q}\right)}{\sin \theta_0}, \quad (\text{B7})$$

$$D_k = 2 \sin\left(\frac{(2k-1)\pi}{2M}\right), \quad (\text{B8})$$

$$A_k = \frac{1 + (d_E/2)^2}{D_k d_E/2}, \quad (\text{B9})$$

$$W_k = B_k + \sqrt{B_k^2 - 1}, \quad (\text{B10})$$

$$B_k = \frac{D_k}{d_k} (d_E/2), \quad (\text{B11})$$

$$\theta_{1k} = 2 \tan^{-1} \left\{ \frac{\tan(\theta_0/2)}{W_k} \right\}, \text{ and } (\text{B12})$$

$$\theta_{2k} = 2 \tan^{-1} \{ W_k \tan(\theta_0/2) \}, \quad (\text{B13})$$

where

$$\theta \equiv 2\pi f / f_s \quad \theta_0 \equiv 2\pi f_0 / f_s. \quad (\text{B14})$$

Figure B4 shows the cascaded bandpass gain and phase response for a 4th order ($M = 2$) bandpass Butterworth filter with $f_s = 11025$ Hz and $Q = 0.25$ for $f_0 = 30$ Hz (solid line); $f_0 = 100$ Hz (thin solid line); $f_0 = 300$ Hz (dashed line); and $f_0 = 1000$ Hz (dotted line). Figure B5 is identical to Figure B4, but with $N = 12$ ($M = 6$) and $Q = 1$.

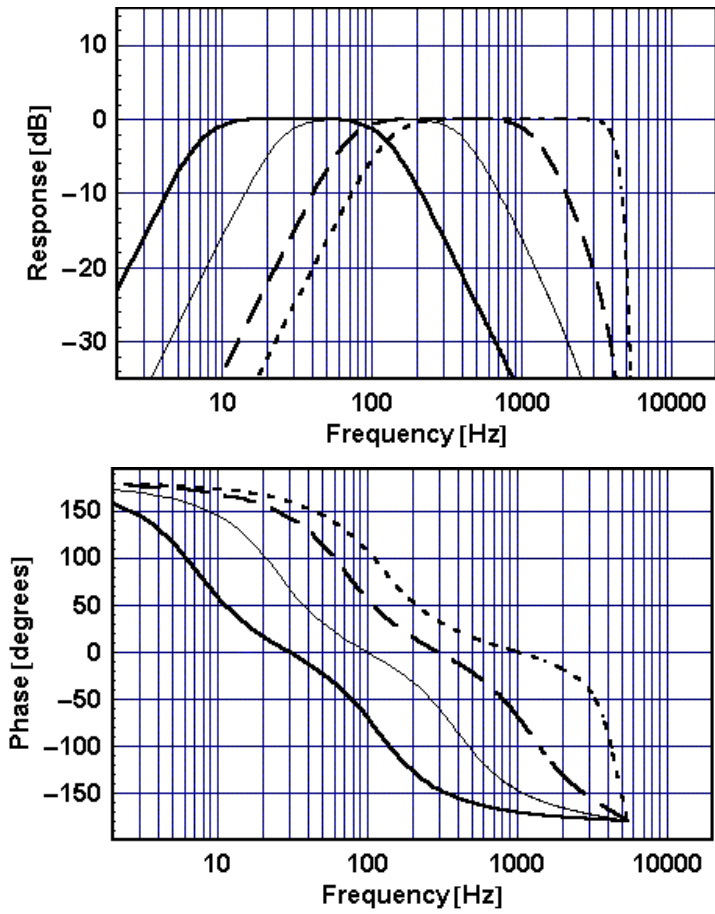


Figure B4. Gain (top panel) and phase response (bottom panel) of digital 4th order ($M=2$) bandpass Butterworth filter with $f_s = 11025$ Hz and $Q = 0.25$. Plots are shown for $f_0 = 30$ Hz (solid line), $f_0 = 100$ Hz (thin solid line), $f_0 = 300$ Hz (dashed line), and $f_0 = 1000$ Hz (dotted line).

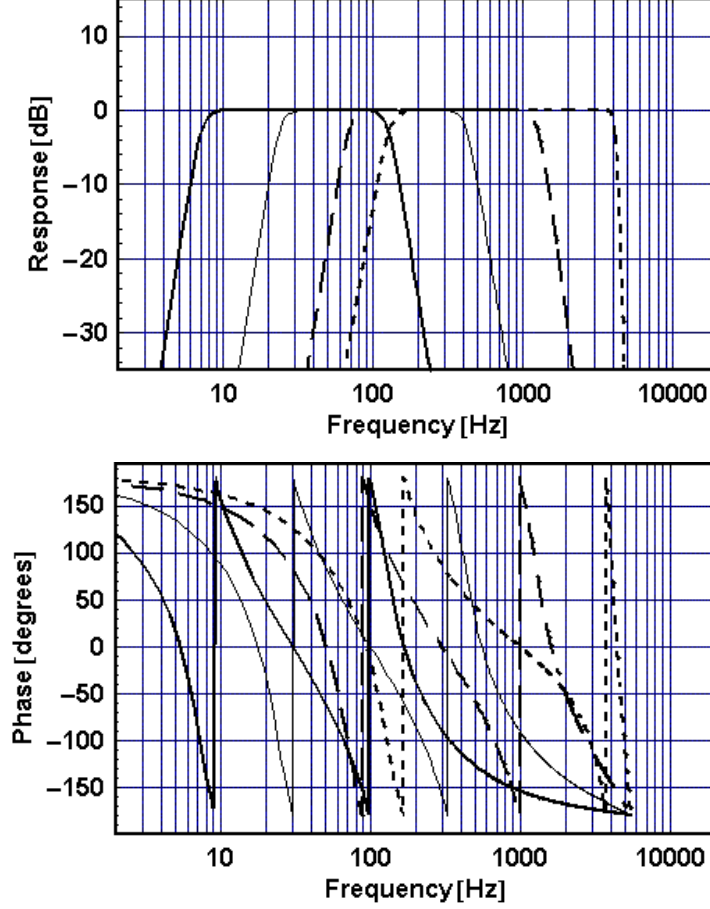


Figure B5. Gain (top panel) and phase response (bottom panel) of digital 12th order ($M=6$) bandpass Butterworth filter with $f_s = 11025$ Hz and $Q = 1$. Plots are shown for $f_0 = 30$ Hz (solid line), $f_0 = 100$ Hz (thin solid line), $f_0 = 300$ Hz (dashed line), and $f_0 = 1000$ Hz (dotted line).

Figures B4 and B5 were generated using the transfer function $H(z)$ from Equation (B2b) and the coefficient formulas of Equations (B3) – (B14). The gain and phase are computed directly from the *magnitude* and *argument* of $H(z)$ by setting $z = e^{2\pi j f / f_s}$:

$$G(f) = \left| H\left(e^{2\pi j f / f_s}\right) \right|, \quad (\text{B15a})$$

$$\phi(f) = \frac{180}{\pi} \tan^{-1} \frac{\text{Im}\left[H\left(e^{2\pi j f / f_s}\right)\right]}{\text{Re}\left[H\left(e^{2\pi j f / f_s}\right)\right]}. \quad (\text{B15b})$$

The steepness of the magnitude response increases with the order of the filter, and approaches a straight line on a log-log plot (or *power-law* on a linear-linear plot):

$$G(f) \rightarrow \begin{cases} f^{-N/2} & f_0 \ll f \ll f_n \\ f^{N/2} & f \ll f_0 \\ 0 & f \rightarrow f_n \end{cases}; \quad \phi(f) \rightarrow \begin{cases} -M \frac{\pi}{2} = -N \cdot 45^\circ & f_0 \ll f \leq f_n \\ M \frac{\pi}{2} = N \cdot 45^\circ & f \ll f_0 \end{cases}. \quad (\text{B16})$$

Equation (B16) corresponds to the familiar N th order bandpass filter stopband response approximation of $-3N$ dB/octave or $-10N$ dB/decade, when f is much less than or much greater than the center frequency, as well as much less than the Nyquist frequency. As f approaches the Nyquist frequency, the filter roll-off steepness increases and the gain becomes exactly zero when $f=f_n$. In some ways, this characteristic of the digital bandpass filter (also true with the lowpass filters) gives an extra boost of stopband suppression as compared to the equivalent analog filter.

Since by convention, as in the analog case of the previous section, a phase angle is defined to be in the range of -180° to $+180^\circ$, Equation (B16) should be modified to reflect this convention

$$\varphi(f) \underset{f \rightarrow 0}{=} \begin{cases} 0 & \text{for } \frac{M}{2} \text{ even} \\ \pi & \text{for } \frac{M}{2} \text{ odd} \end{cases}, \text{ and} \quad (\text{B17a})$$

$$\varphi(f) \underset{f \rightarrow f_{ny}}{=} \begin{cases} 0 & \text{for } \frac{M}{2} \text{ even} \\ -\pi & \text{for } \frac{M}{2} \text{ odd} \end{cases}. \quad (\text{B17b})$$

The gain and phase at the center frequency for all N is

$$G(f_0) = 1, \text{ and} \quad (\text{B18a})$$

$$\phi(f_0) = 0^\circ. \quad (\text{B18b})$$

The quality factor Q is inversely proportional to the frequency bandwidth Δf of the gain response curve

$$Q \equiv \frac{f_0}{\Delta f} = \frac{\theta_0}{\Delta \theta}. \quad (\text{B19})$$

where $\Delta f = f_2 - f_1$ and $\Delta \theta = \theta_2 - \theta_1$. The normalized center frequency θ_0 is related to the normalized edge frequencies θ_1 and θ_2 by

$$\tan(\theta_0/2) = \sqrt{\tan(\theta_1/2)\tan(\theta_2/2)}, \quad (\text{B20})$$

where $\theta_0 = 2\pi f_0 / f_s$, $\theta_1 = 2\pi f_1 / f_s$, and $\theta_2 = 2\pi f_2 / f_s$.

The edge frequencies f_1 and f_2 are computed using an iterative method. Figure B6 shows the gain response of several N th order Butterworth bandpass filters with $Q = 0.33$, $f_0 = 300$, and $f_s = 11025$ Hz. Using Equations (B21a) and (B21b), the edge frequencies are computed for this case using several values of filter order $N = 2M$. Note that in all cases, the response curves intersect at a common point corresponding to the -3 dB gain (or gain = $2^{-1/2}$), at the edge frequencies f_1 and f_2 .

$$f_1 = \frac{f_s}{\pi} \tan^{-1} \left\{ \frac{\tan^2(\pi f_0 / f_s)}{\tan[(f_1 + f_0 / Q)\pi / f_s]} \right\}. \quad (\text{B21a})$$

$$f_2 = \frac{f_s}{\pi} \tan^{-1} \left\{ \frac{\tan^2(\pi f_0 / f_s)}{\tan[(f_2 - f_0 / Q)\pi / f_s]} \right\}. \quad (\text{B21b})$$

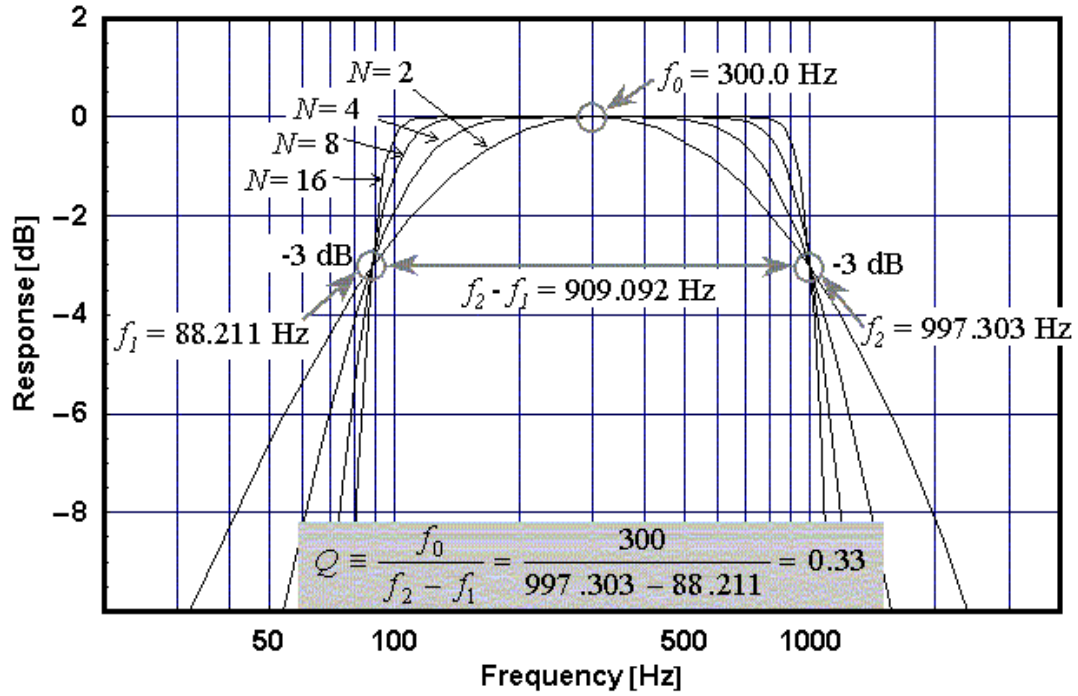


Figure B6. Gain response of 2nd, 4th, 8th, and 16th order Butterworth bandpass filters with $Q = 0.33$, $f_0 = 300$, and $f_s = 11025$ Hz.

As with the second order bandpass filter, the Q has a finite limit on the low end, as shown in Equation B22. There is no theoretical upper limit on Q , with the second order IIR bandpass filter; however, issues concerning roundoff errors and other problems with finite size numbers generally lead to a practical upper limit on Q .

$$Q > f_0 / f_n \tag{B22}$$

List of Abbreviations and Acronyms

Term	Description
AMU	Applied Meteorology Unit
BP	Bandpass
CCAFS	Cape Canaveral Air Force Station
CEM	Contour Error Method
FIR	Finite Impulse Response
IIR	Infinite Impulse Response
ISAN	Isentropic Analysis
KSC	Kennedy Space Center
LDT	Local Daylight Time
LP	Lowpass
LSBO	Land Sea Breeze Oscillation
METAR	Aviation Routine Weather Report
MHz	Mega-Hertz
MM5	Mesoscale Model version 5
NCAR	National Center for Atmospheric Research
NCEP	National Centers for Environmental Prediction
NWP	Numerical Weather Prediction
RAMS	Regional Atmospheric Modeling System
SB	Sea Breeze
UTC	Universal Time Coordinated

NOTICE

Mention of a copyrighted, trademarked or proprietary product, service, or document does not constitute endorsement thereof by the author, Dynacs Inc., ENSCO Inc., the AMU, the National Aeronautics and Space Administration, or the United States Government. Any such mention is solely for the purpose of fully informing the reader of the resources used to conduct the work reported herein.